Universiteit Utrecht

Mantle geochemistry indicates original magmatic heterogeneity was unaltered during subduction infancy: Insights from the Mont Albert ophiolite complex (Québec, Northern Appalachians)

Hester Smit

March 2023

Submitted in partial fulfilment of the Master of Science in Earth Structure and Dynamics.

Acknowledgements

This thesis is written as part of the Master of Science degree in Earth Sciences, programme Earth Structure and Dynamics, at Utrecht University. It has come together under close supervision of assistant professor Alissa Kotowski.

First and foremost a very special thanks to assist. Prof. Alissa Kotowski, who guided me through this project. This project was a very special adventure going from retrieving rocks from the field, processing them in the lab and writing this thesis. I very much enjoyed the process and appreciate the chance given. A second word of gratitude goes out to associate professor Oliver Plümper, who took on the role of second supervisor. I'd like to mention Jippe van broekhoven and Tim van de Wurf with whom I worked closely together. We supported each other throughout the process and I am thankful to them for the fun days during and outside of office hours. For this research fieldwork was conducted in Québec, Canada. A major thanks to Parc National de la Gaspésie for granting a research permit, and to the whole fieldworksquad, Jamie Kirkpatrick, Mark Coleman, Matt Tarling, and Francois Fournier-Roy, for their helpful insights in the field and good conversation over delicious field coffee. I wish to show my appreciation for to all the lab technicians who helped perform the chemical analyses and a special thanks to Eric Hellebrand who helped me enormously with data processing and was always happy to chat, and Helen de Waard for help on the laser. Furthermore I'd like to mention Austin Arias, Emily Cooperdock and Lisa Eberhard with whom I had fruitful discussions. Lastly, this project would not have been possible without the generous support of the Olaf Schuilingfonds.

Abstract

Subduction initiation is a necessary prerequisite to generate Earth-like plate tectonics. However, it is not yet understood how elements begin to cycle through the lithospheric mantle during subduction infancy and how they initially affect mantle composition and thus slab-mantle interface rheology. Progressive development of a “mature” forearc mantle wedge above a subducting slab typically results in melt and fluid metasomatism in the upper plate’s lithospheric mantle, often thought to drastically change original (micro)structures and rock chemistry. Ophiolitic complexes provide a window into the chemical and structural evolution during the earliest stages of formation of a subduction interface in the supra-subduction zone (SSZ) mantle wedge. The Mont Albert Ophiolite Complex (Québec, Northern Appalachians, Canada) is an ideal locality to study the slab-mantle interface, because the contact zone between the down-going crust (Iapetus Ocean) and upper-plate lithosphere (Laurentia) of an Ordovician subduction zone is well-exposed. Focusing on the upper plate mantle, I combined field-based structural observations, optical and electron microscopy, and bulk rock major and trace element geochemistry to investigate the structural and metasomatic changes occurring in the immediate hanging wall during subduction initiation. At the “Mantle Wall” locality, serpentinized peridotites exhibit a strong moderately dipping foliation across a ~100 m structural section, in an apparently in-tact orientation relative to paleo-subduction and obduction. Microstructural observations demonstrate the degree of serpentinization decreases with structural height above the paleo-plate interface. Geochemical tracers including Cr#, Rare Earth Elements (REE) and Fluid Mobile Elements (FME) demonstrate that the tectonic setting of original mantle was in an abyssal setting, the extent of melt extraction from the mantle is heterogeneous (between 5-15% over ~60 m of structural section), and serpentinite metasomatism did not impart a systematic chemical overprint to the rocks. I infer that the peridotites underwent limited melt-reactions and limited FME-enrichment during serpentinization *after* subduction initiation, and the differences in apparent depletion pre-date subduction. Preservation of original lithospheric complexity in an infant subduction zone demonstrates that mantle wedge chemistry is heavily dependent on the maturity of the fore-arc. The late-stage serpentinization opposes the notion that serpentine is essential in subduction initiation. This study rather illuminates the preservation of original mantle heterogeneity in the form of original compositional layering, which may play a role in strain localization during subduction initiation. Combining chemical analysis with structural field context appears critical to accurately characterize the composition of a SSZ mantle wedge and understand its evolution.

Contents

Acknowledgements 2
Abstract 3
Contents 4
Figures 6
Tables 10
1. Introduction 11
1.1 Melt-rock interactions in subduction zones 12
1.2 Fluid cycling in subduction zones and chemical signatures of serpentinization 13
2. Geological setting 15
2.1 Overview of the Appalachian Mountains 15
2.2 Geology of the Gaspé Peninsula 16
2.2 Mont Albert 18
2.2.1 Metamorphic sole 18
2.2.2 Mantle peridotite 19
3. Methods 20
3.1 Sampling strategy 20
3.2 Analytical techniques 21
3.2.1 Optical and Electron microscopy 21
3.2.2 Bulk rock major element analysis via X-Ray Fluorescence (XRF) 22
3.2.3 Bulk rock trace element analysis via laser ablation-inductively coupled plasma-mass spectrometry (LA-ICP-MS) 22
3.2.4 In-situ mineral composition via Electron Micro Probe Analyzer (EMPA) 23
4. Results 24
4.1 Outcrop to microscale: structural and petrologic observations 24
4.1.1 Mantle Wall 24
4.1.1.1 Unit 1: contact zone/ultramylonitic serpentinite 25
4.1.1.2 Unit 2: mylonitic serpentinite 29
4.1.1.3 Unit 3: Proto-mylonitic serpentinite 30
4.1.1.4 Unit 4: porphyroclastic peridotite 30
4.1.2 NE-Arrêt 31
4.1.3 Mont Olivine 32
4.2 Geochemical results 34

4.2.1 Major elements (bulk rock) 34
4.2.2 Trace elements (bulk rock) 38
4.2.3 Mantle rock mineral composition (In-situ) 42
5. Discussion 46
5.1 Chemical constraints on tectonic setting of peridotite and sole formation 46
5.2 Trends in melt depletion with structural distance from the sole-mantle contact 49
5.3 No further melt extraction or infiltration following subduction initiation 50
5.4 Limited fluid mobile element overprinting during serpentinization 51
5.5 Implications for strain localization during subduction initiation 54
5.7 Future work 55
6. Conclusion 56
References 57
Supplementary Figures and Tables 66

Figures

Figure 1 Geological map of Northern Appalachians. Taken from Tremblay and Pinet (2016). 17
Figure 2 Lithology and basic structures of Mont Albert. Sampling locations for this study are indicated in yellow squares. Modified from Dubacq, 2018. 19
Figure 3 Location of sample selection. A) Roughly strike-parallel view of Mantle Wall showing south-dipping foliation and the exact sampling locations of Mantle Wall transect. Black lines indicate separation of rock units. B) GoogleEarth aerial view of Mantle Wall with geologic units, structural orientation and an approximation of the contact that runs between metamorphic sole and mantle wedge. Dark red is metamorphic sole, orange is contact mylonite and yellow is serpentinized peridotite. Green and grey is vegetation and gravel. Note: Sample KMA22-48 and KMA22-50 have been collected 2 km to the East outside of this view. 21
Figure 4 stratigraphic column of rock units found on Mantle Wall. Level of serpentinization and mineralogy is indicated. 25
Figure 5 a) Estimated contact (yellow line) between metamorphic sole and mantle rock on Mantle Wall foliation dipping South, b) Contact (yellow line) between metamorphic sole and mantle rock on NE-Arête, c) sole rock amphibolite containing quartz veins, d) rock unit 1 – mylonitic serpentinite e) iron rich shear bands in contact rock and rock unit 1, f) white lens in rock unit 2, g) chromite layer in rock unit 2, h) pink layering in rock unit 3 with foliation parallel chrysotile vein i) porphyroclastic peridotite, j) dunite channel between red lines, foliation in black lines, k) fresh peridotite from Mont Olivine 27
Figure 6 Microscopy of Mantle Wall rock units I) PPL thin section of unit 1 - contact rock; Ia) Hematite network (PPL), Ib) altered chrome-chlorite spinel with chlorite aureole (PPL); II) PPL thin section of unit 4; IIa) ribbon serpentine mesh from pink banding with original ol grains in yellow (XPL); IIb) bastite with crosscutting talc veins (XPL); 11c) chrysotile vein in serpentine mesh (PPL); III) PPL thin section NE-Arrêt porphyroclastic peridotite; IIIa) Relict olivine grains with serpentine near grain boundary (XPL); IIIb) former opx grains, replaced with coarse grained ol and opx (XPL); IIIc) unaltered and altered spinel grains in a olivine/serpentine mesh (PPL)

Serpentine is heavily affected by browning, which previously observed and defined by Albers et al. (2020) as a late stage fluid alteration. 28
Figure 7 Microscopy from Mont Olivine a) orthopyroxene with bending in clinopyroxene exsolution lamellae (XPL) b) undulose extinction in original olivine (XPL) c) PPL image of thin section of peridotite d) EBSD map of section of thin section 29
Figure 8 Ternary diagram for sample KMA20, which is a representative for fresh peridotite. Black dot represents the composition of peridotite. 33
Figure 9 Levels of L.O.I. and Ferrous and Ferric iron content normalized to MgO. Datapoints are set against their distance relative to the contact. 35
Figure 10 Ratios of MgO/SiO2 and Al2O3/SiO2 throughout the sample transect. Red squares are the fully serpentinized samples closest to the contact transitioning into blue which represent the partly serpentinized samples. Fresh peridotite is represented as triangles in green. Global dataset collection from Deschamps et al. (2013) are shown in grey circles as comparison. The blue bubble under the terrestrial array is defined for abyssal peridotites by (Niu, 2004). The dark blue line indicates the 'terrestrial array', which represents Earth's melting array from depleted mantle (Jagoutz et al., 1979). Moving up or down from the terrestrial array often indicates carbonation or seawater alteration respectively. Depleted and primitive mantle values are taken from McDonough & Sun (1995). 36
Figure 12 multi-element spider diagram with selected elements like Deschamps (2013). Gloss is taken from has been plotted for comparison to determine on sediment influx. Primitive mantle values and depleted mantle (DM) is taken from McDonough & Sun (1995). 40
Figure 11 REE pattern together with the melting trends estimated from Niu (2004). They represent the melting array from a depleted MORB mantle, assuming fractional melting. DM and C1 chondrite values are taken from Mcdonough and Sun (1995).....40
Figure 13 a) good correlations between MgO wt% and yb (bulk rock)*; b) moderate correlations between MgO wt% and Ce (bulk rock)*; c) correlations between Dy and Ti (bulk rock)*; d) correlations between Ho and Ti (bulk rock)*; e) correlations between Nd and Nb (bulk rock)*; f) orthopyroxene composition Al_2O_3 and Mg# (wt%), where porphyroclast concentration plot in abyssal bubble; g) spinel composition TiO_2 and

Al_2O_3 (wt%) fall into abyssal bubble; h) bulk rock major element Al_2O_3 and trace element Yb show positive correlations and indicate similar mobility in melt processes.....41
Figure 14 Core/rim composition of Cr-spinel in a) KMA20 (peridotite) and b) KMA22-47 (serpentinite). Yellow dotted line in b) indicates areas of Cr-spinel alterations into a chrome-chlorite. 44
Figure 15 a) Combined core/rim composition of spinel minerals in b) KMA20 (top right, peridotite) and c) KMA22-47 (bottom right, serpentinite). Cores are plotted in red diamonds and rims in yellow circles. Note that the x-axes are plotted from high to low. Typically fore arc samples plot above Cr# =0.6 and abyssal below Cr# =0 (Ahmed & Surour, 2016; Gamal El Dien et al., 2019).....44
Figure 16 Spinel Cr# versus. Olivine Mg#. Mantle Wall samples are indicated by red diamonds and are compared to lherzolites/harzburgites from Oman taken from (Khedr et al., 2014; Takazawa et al., 2003) and harzburgites from Bay of Island, Newfoundland from (Stern, 2013). Fields for SSZ mantle wedge and abyssal indicate where the average global datasets fall. Figure modified from Arai (1994) and Khedr et al. (2014). 47
Figure 17 Multi-element and REE patterns compared to compiled datasets by Deschamps 2013. Mont Albert concentrations are shown in black. The abyssal dataset can be separated into two subsets corresponding to depleted mantle and refertilized abyssal composition due to melt-rock interactions (indicated in orange field). 48
Figure 18 Zoom in on difference in FME concentrations between sample with the highest level of serpentinization (KMA22-03) and fresh peridotite (KMA20). Topright: A selection of FME (Cs, Rb, Ba, U, Pb, Sr – ordered on increasing compatibility) show the very limited difference in element concentrations between the structurally lowest serpentinite (near 100 % serpentine by volume) and peridotite.....52
Figure 19 Trace element concentrations and ratios plotted in discriminatory plots from Peters (2017). Datapoints are compared to mid oceanic ridge (MOR – in black) and fore arc (FA – in blue) setting.....53
Figure 20 Conceptual image portraying the evolution of 1) heterogeneous abyssal lithosphere in MOR setting; 2) after subduction initiated. The estimated location of Mont Albert, with sole

rock and Mantle Wall sequence is indicated in white box and yellow. Mont Albert is indicated with known temperature and depth constraints. Note that more heterogeneity in the oceanic lithosphere is likely, and only the heterogeneity that is confirmed in this research is indicated in this illustration.....54

Tables

Table 1 Sample suite organized by their lithology and with increasing distance from the contact. All samples have been used for optical microscopy. 21
Table 2 Major and trace element concentrations 37
Table 3 Mineral compositions of olivine, spinel, orthopyroxene and clinopyroxene. 45

1. Introduction

Serpentinized ultra-mafic rocks are often found in hyper-extended margins, mid-ocean ridge spreading centers, exhumed subduction complexes, and ophiolites, and can form a collection of clues of the geological history of a region. In subduction zones, serpentinites have clear mechanical and metasomatic significance. They are thought to be pre-requisites for strain localization facilitating subduction initiation (Hilairet et al., 2007), they facilitate buoyancy-driven exhumation of high-pressure metamorphic rocks (Bebout & Penniston-Dorland, 2016; Hirth & Guillot, 2013), and they take up water and fluid-mobile elements that affect global geochemical cycling and arc volcano geochemistry (K. H. Hattori & Guillot, 2003). However, the spatial and temporal scales over which mantle metasomatism processes operate, and what influence they have on mantle composition as a whole, remains speculative. In recent years, the composition of peridotites and serpentinites have been used to determine the geologic evolution of a rock through the mantle (Bebout & Penniston-Dorland, 2016; Deschamps et al., 2013; Scambelluri et al., 2004). As such, the tectonic evolution can be recognized by a characteristic chemical fingerprint, which is subject to change due to melt-rock interaction, deformation, and overprinting of fluid metasomatism (Scambelluri et al., 2004; Ulmer & Trommsdorff, 1995). Current research on major and trace element patterns is often based on well-established, mechanically 'mature' subduction zones. Most studies consider the mantle wedge chemistry as a whole, however, processes occurring in the mantle wedge away from the plate interface (i.e., at sub-arc positions) vs. those occurring in the "cold" mantle wedge corner are significantly different. Melt processes often occur at irregular intervals and in heterogeneous spatial distributions in sub-arc and fore-arc locations (Ulmer, 2001). In this context, infant subduction zones are especially intriguing, since they should preserve the chemical signatures of the very first steps of melt and fluid cycling occurring in the (proto-forearc) mantle wedge.

An ideal location to study the extent of fluid flow in a young mantle wedge and its consequences on melt depletion is Gaspésie National Parc, Québec, Canada. Here, the incomplete ophiolite body of Mont Albert records a thick structural section of serpentinized upper plate mantle that is in direct tectonic contact with a thin structural unit of paleo-subducting crust (Dubacq et al., 2019). Bulk rock major and trace elements of Mont Albert's (hydrated) peridotites can provide the first order interpretation of its tectonic evolution. Original mineral composition can give insights in pre-subduction protolith formation as melt-rock interaction signatures are especially well preserved in trace elements and original mineral composition (Arai, 1994; De Hoog et al., 2009; Hellebrand et al., 2001). In addition to melt signatures, hydrated peridotites or serpentinites are characterized by fluid-alteration signatures. Serpentinites can carry up to ±16%

of structurally-bound H_2O (average ~13%) (Deschamps et al., 2013; Kodolányi et al., 2012) and are sensitive to geochemical tracers that reveal something about the rock-fluid interactions, such as where the water originated from and when (in a relative sense) serpentinization occurred (Bebout & Penniston-Dorland, 2016). It is a complex system and active research is striving to differentiate between types of serpentinite formation.

This study will contribute to our understanding of the significance of serpentinites in subduction plate boundary settings by answering the question: "**What are microstructural and geochemical signatures of melt-rock interaction during lithosphere formation and how is that signature modified by fluids during subduction initiation?"** This study will provide a first order structural and chemical analysis of an infant supra-subduction zone mantle wedge in order to provide tectonic context for its pre-subduction configuration and serpentinite formation during subduction. Ultimately, results from this work have led me to develop the hypothesis that the age of a subduction zone relative to subduction initiation and the original mantle compositional and structural heterogeneity significantly influence its chemical portfolio, which is not typically discussed in serpentinite literature, but has broad-reaching implications for mechanisms of subduction initiation.

1.1 Melt-rock interactions in subduction zones

Supra-subduction zone mantle wedges experience increased partial melting due to introduction of volatiles from the subducting slab (Yoder & Tilley, 1962). What exactly controls melt generation and the formation of melt pathways is under heavy debate and has been explored with chemical and seismic analyses (Hicks et al., 2023; Stuart et al., 2018). While partial melting was previously explained by batch or fractional melting along localized pathways, it is now suggested melt migration also occurs at much smaller scales along grain boundaries (Stuart et al., 2018). The formation of melt is heavily influenced by temperature, pressure and mantle composition, thus much research is currently focusing on the thermal structure of the mantle wedge (Wada et al., 2011). Based on assumptions of thermal structure, the upper-plate mantle wedge at structural positions away from the plate interface is expected to experience higher temperatures and more partial melting than in the stagnant cold corner. This is an important distinction when discussing major and trace elements signatures in the mantle. While melt-rock interaction is typically indicated by microstructural observations (e.g. interstitial melt pockets and replacement reactions), it has become increasingly common over the last two decades to interpret melt-rock interaction from geochemical signatures (Niu, 2004; Plank & Langmuir, 1993; Stuart et al., 2018). Geochemical tracers like spinel Cr# and rare earth elements (REE) concentrations provide useful

constraints on the tectonic setting of original protolith formation and the percentage of melt depletion (Hellebrand et al., 2001; Warren, 2016). The use of geochemical tracers is based on the premise that elements are either mobilized by melt processes, fluid processes, or both. This is all controlled by element compatibility, where elements with certain ionic charges and/or radii are more likely to be removed by a passing melt or fluid. For example, High Field Strength Elements (HFSE) are considered fluid immobile, but Light Rare-Earth Elements (LREE) and Large Ion Lithophile Elements (LILE) are more susceptible to fluid mobilization as they are more incompatible in parent rock mineralogies. Therefore, HREE patterns are considered strong indicators for extent of melt depletion and tectonic setting of the mantle, whereas LREE and other fluid-mobile elements are indicators of fluid metasomatism.

1.2 Fluid cycling in subduction zones and chemical signatures of serpentinization

Serpentine exists as three polymorphs, antigorite, chrysotile, and lizardite, that all have a broad Pressure-Temperature (P-T) range of stability. Antigorite is the high-P and high-T polymorph, and is stable at depths approaching 100-170 km and temperatures up to 600-700 °C (Bromiley & Pawley, 2003; Wunder & Schreyer, 1997). The varieties lizardite and chrysotile are stable at lower temperature of T < 300-400 °C and often form at shallower depths reaching max 50-70 km (Guillot et al., 2015; Schwartz et al., 2013). Furthermore, prograde metamorphism can lead to dehydration of serpentine and formation of secondary olivine (e.g., Plümper et al., 2017), which can create complex textures characterized by multiple overprinting polymorphs or stages of hydration and dehydration, which often poses the challenges in interpreting serpentinization histories and their individual chemical fingerprints.

Serpentinizing fluids generally originate from seawater, metamorphic dehydration reactions or sediment pore fluid (Prigent, Guillot, Agard, Lemarchand, et al., 2018; Scambelluri et al., 1995; J. M. Warren & Shimizu, 2010). In subduction zones, each of these volatile sources can be introduced to the lithospheric mantle where they migrate as free fluid, get stored as OH- in hydrous phases (chlorite, serpentine), or exist as H point defects in nominally anhydrous minerals (olivine, pyroxene) (Deschamps et al., 2013). Different sources of serpentinizing fluids have characteristic element concentrations which can be sequestered into the mantle. Thus, the specific source of a serpentinizing fluid influences global geochemical cycling and arc chemistry (Plank and Langmuir, 1993).

Similar to melt signatures, we can leverage the characteristic geochemical tracers that characterize fluid sources and environments. Due to fluid cycling, serpentinized mantle rocks form a major reservoir for fluid-mobile elements (FME) (Bebout & Penniston-Dorland, 2016;

Deschamps et al., 2010; Niu, 2004; Scambelluri et al., 2004). Fluid mobile elements is a collective name for elements that are prone to be mobilized in a hydrated environment. They include semi-volatile (As, Sb), light elements (Li, B) and Large Ion Lithophile Elements (Cs, Rb, Ba, U). When present, these elements can infer a lot about possible sediment influx, tectonic setting of serpentine formation, geochemical cycling and P-T history. For example, U tends to be enriched in a seawater fluid, whereas Cs and Rb occur in higher concentrations in fluids derived from crustal dehydration (Peters et al., 2017).

Considering the processes that mobilize the aforementioned geochemical tracers, serpentinites can be divided into three categories:

a. Abyssal/Oceanic - These serpentinites are often produced at low-temperatures on the seafloor at slow spreading ridges or by infiltration in major fault and fracture zones at fast spreading ridges. Seawater can infiltrate the crust and reach levels of ±7 km in the mantle (Evans et al., 2013). Hydrothermal activity can lead to higher temperature oceanic serpentinites (350°C). Examples of oceanic serpentinites are fast spreading Hess Deep (Kodolányi et al., 2012), seafloor hydrated MARK and ODP Leg 209 (Kodolányi et al., 2012; Paulick et al., 2006) and Atlantis massif-IODP exp. 304-305 (Delacour et al., 2008). In trace element spider diagrams, abyssal/oceanic serpentinites exhibit a range of melt depletion in HREE concentrations, local enrichments in FME, and coupled negative Ce and positive Eu anomlies when normalized to primitive mantle (Deschamps et al., 2013).
b. "Subducted" Serpentinites – Previously hydrated lithosphere can subduct and form subducted serpentinites. For example, when a hydrated slab subducts into the mantle, the slab and sediments on the slab are dehydrated and typically induce a seawater and sediment chemical signature during serpentinite formation (Plank & Langmuir, 1998). Examples of subducted serpentinites are Erro Tobbio, Italy (Plümper et al., 2017; Scambelluri et al., 1995), Cerro Del Almirez in Spain (Jabaloy et al., 2015), and the Feather river ophiolite, California (Li & Lee, 2006). However, this category is difficult to use as a 'smoking gun' chemical fingerprint because the trace element patterns — characterized by flat HREE patterns and extremely variable FME concentrations — overlap with similar signatures recorded by serpentinites formed along passive margins. This issue arises from the unclear structural or tectonic context for many of the serpentinites used to create the global compilations (Deschamps et al., 2013).
c. Mantle Wedge – When a hydrated subducting slab reaches sub-Moho mantle depths, it can dehydrate and cause fluids to move into the overlying mantle wedge. This leads to

hydration of the mantle wedge and causes increased partial melting and arc magmatism (Evans et al., 2013; Mallik et al., 2016). Examples are Mariana fore-arc (Kodolányi et al., 2012; Savov et al., 2005), Indus suture zone in Himalaya (K. Hattori & Guillot, 2007) and the Rio San Juan Complex, Dominican Republic (Saumur & Hattori, 2013). A potentially diagnostic trace element signature in this category is extreme and consistent depletion in all REE, yet LILEs exhibit similar patterns as the more depleted category of abyssal/oceanic serpentinites.

2. Geological setting

2.1 Overview of the Appalachian Mountains

The Appalachian Mountain range is a product of the Taconian, Devonian and Acadian Orogeny and spans from present-day North Carolina, into Québec and Newfoundland, to western Ireland, Great Britain, and Scandinavia. The mountain belt formed from the closure of the Iapetus and Rheic oceans and episodic accretion of Gondwanan-derived microcontinents to the paleo-Laurentian margin throughout the Paleozoic (Tremblay & Pinet, 1994). The Appalachians are currently exposed as different accreted tectonic terranes younging eastward toward the present-day Atlantic margin. During the Taconian orogeny, the Ordovician (~ 500-450 Ma) closure of the Iapetus ocean resulted in the accretion of tectonic terranes to Laurentia (proto-North America) (Staal & Barr, 2012). The accreted terranes currently form the Humber zone and Dunnage zone, which respectively comprise the continental paleo-margin of Laurentia, and the syn-orogenic sediments and ophiolite complexes (Malo et al., 2008; M. Perrot et al., 2017; Tremblay & Pinet, 2016). In the Northern Appalachians, the Taconian orogeny is expressed as steeply dipping NW folding and thrusting. The metamorphic rocks are mainly of greenschist facies, reaching greenschist-amphibolite facies in the Humber zone. The Dunnage zone is characterized by SE verging refolded folds. Continued convergence led to a second accretionary episode during the Silurian (~ 440-423 Ma), where peri-Gondwanan Ganderia accreted to the Laurentia margin, closing the Acadian seaway (Staal & Barr, 2012). Metamorphism and deformation of convergence during the Salinic orogeny is only locally expressed in the Northern Québec peninsula, while to the South, SE verging backthrust faults are recorded. The Salinic orogeny was followed by an extensional rifting event during the Late Silurian. Extensional deformation structures have been recorded in segments of the Québec peninsula with normal faulting and syn-kinematic wedge formation (M. G. Perrot et al., 2021). During the Late Silurian to late Devonian (~ 420-400 Ma),

the Acadian orogeny occurred during which the peri-Gondwanan Avalonia and Meguma accreted onto Laurentia. Acadian deformation is recorded as NW verging, SE dipping folds, and reverse faults (Staal & Barr, 2012). The final closure of the Rheic ocean led to the ultimate assemblage of Laurentia and Gondwana and creation of supercontinent Pangea, during the Carboniferous-Permian Alleghian orogeny (~ 20-260 Ma) (Staal & Barr, 2012). Opening of the Atlantic Ocean reactivated the late-Paleozoic suture, in which the accreted Gondwanan margin rifted away from eastern North America in the Mesozoic and this process continues through present-day. While younger extensional and compressional tectonic events have been recorded along the Northern Appalachians, most deformation and metamorphism is Ordovician-Silurian in age. The preservation of these older deformation structures and older metamorphic signatures provides a perfect opportunity to study Taconian and Acadian deformation and metamorphism.

2.2 Geology of the Gaspé Peninsula

The Gaspé peninsula, southeast of Québec, is mainly composed of NE-SW slivers of Taconian Humber and Dunnage terranes exposed throughout unconformable Silurian and Devonian sediment deposits (Figure 1). The Humber and Dunnage zone are bound by the Appalachians structural front in the North and an unconformity in the South (M. G. Perrot et al., 2021). The zones are separated by the Baie-Verte-Brompton Line (BBL), which was originally thought off as a suture between continent and oceanic material (Tremblay & Pinet, 1994; Williams, 1979). In recent years, this idea has been opposed by Tremblay & Pinet (2016) who argue the BBL rather consists of a complex fault zone and is not just related to the plane of obduction.

North of the BBL is the Humber zone, which comprises continental rocks from the Laurentian margin and is separated into the external and internal zone by an Acadian strike-slip fault. The internal zone contains Upper Neoproterozoic – Early Middle Ordovician metasedimentary schists and Neoproterozoic – Cambrian subalkaline to tholeiitic metabasalts. The metamorphic rocks reach Taconian greenschists facies, with local exposures of greenschists-amphibolite facies. Deformation is expressed as multiple phases of folding. The external zone comprises Upper Neoproterozoic-Lower Ordovician margin slope sediments and Middle to Upper Ordovician syn-orogenic flysch deposits. Minor volcanic rocks are exposed throughout the zone. The external zone underwent a low degree of metamorphism and Ordovician deformation is expressed as folding and steeply East dipping faults.

The Dunnage zone is located south of the BBL and consists of ophiolitic, volcanic and sedimentary remains. Located 50 km to the south of Québec, other ophiolites are found such as the Thetford-Mines, Asbestos, and Lac-Brompton ophiolites. These ophiolites are similar in

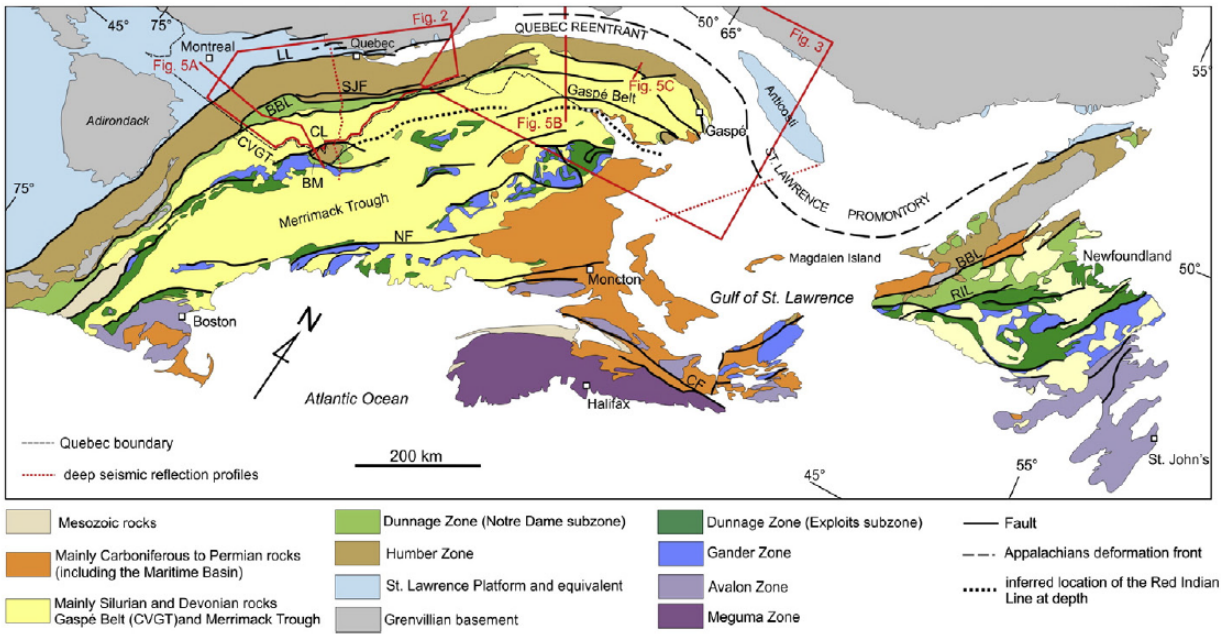

Figure 1 Geological map of Northern Appalachians. Taken from Tremblay and Pinet (2016).

lithostratigraphy and geochemistry and are interpretated to originate from the same fore arc obducted oceanic lithosphere (Tremblay & Pinet, 2016; Whitehead et al., 1995). Emplacement of the Québec ophiolites on Laurentian continental margin and accompanied deformation is dated back to ~475-460 Ma, by $^{40}Ar/^{39}Ar$ dating (Souza et al., 2011; Tremblay et al., 2011; Whitehead et al., 1995). On the Gaspe peninsula, as part of one ophiolitic complex, three ultramafic bodies are located: Mont Paul, Mont du Sud, and Mont Albert of which the latter is especially well preserved. The Gaspé ophiolitic bodies are very similar to the southern ophiolites in lithology and age constraints, where the obduction of Mont Albert is dated back to 459-456 Ma by $^{40}Ar/^{39}Ar$ dating (Malo et al., 2008).

On a larger scale, the Québec ophiolitic bodies are often compared to the Bay of Islands ophiolite, Newfoundland, Canada, and the Semail ophiolite, Oman (Church, 1977; Dallmeyer & Hibbard, 1984; Dewey & Casey, 2013). Similarities in lithology and tectonic evolution have led to numerous comparisons between the three localities. Corresponding age constraints for the Québec and Bay of Islands ophiolites has led to the interpretation of these two being genetically related; obduction of the Bay of islands ophiolite is dated back to ~470 Ma (Dewey & Casey, 2013). For all ophiolites, most analytical work and comparison has been done on the metamorphic sole, as opposed to the mantle rock. Analysis of mantle rock composition show that the geochemistry of Cr-Spinel major, trace, and mineral composition of Semail and Bay of Island

dunites are comparable, while Cr-Spinel trace elements of Thetford mines differ from those in the Bay of Islands ophiolite (Stern, 2013). To this day, no in-depth mantle rock geochemistry comparisons with Mont Albert and the other ophiolitic bodies have been made.

2.2 Mont Albert

Mont Albert, Mont Paul and Mont du Sud together form the Mont Albert ophiolitic complex. Mont Albert is the largest of these three ultramafic bodies. In the South, Mont Albert is bound by a transform SSF fault separating it from the Ruisseau Isabelle Mélange, composed of Cambrian to Ordovician sediments and peridotites. In the North, Mont Albert is separated from the Shick-Shock Group by the Taconian thrust fault contact (Dubacq et al., 2019; Malo et al., 2008; M. Perrot et al., 2017). The Shick-Shock Group consists of metabasalt and metasediments that relate back to the pre-Taconian rifting of the Iapetus ocean (Camiré et al., 1995). Earlier theories on the tectonic evolution of Mont Albert describe it to be a magmatic intrusion, that serpentinized after cooling down (Alcock, 1927; MacGregor & Basu, 1979). This idea got disputed in recent years, where the ultramafic complex is more accurately described as an incomplete ophiolite sequence with a missing crustal component (Beaudin, 1986; Dubacq et al., 2019). Mont Albert consists of a succession of high grade metamorphic rock, interpreted as the sole of a subducting slab, underlaying a serpentinized harzburgitic mantle rock, interpreted as SSZ mantle wedge (Figure 2) (Dubacq et al., 2019; Tremblay & Pinet, 2016).

2.2.1 Metamorphic sole

The high grade metamorphic rock is characterized by amphibolite facies with a maximum thickness of 80-100 m. Foliation orientation is roughly parallel to the peridotite contact. Metamorphic grade and grain size decrease with increasing structural depth away from the peridotite contact; garnet and clinopyroxene bearing amphibolite with a low content of amphibole transitions into a mainly amphibole and plagioclase bearing amphibolite. The sole has been of particular interest to constrain metamorphic conditions. Garnet-clinopyroxene and amphibole-plagioclase thermobarometry performed by Dubacq et al. (2019) show that at the peridotite contact, peak conditions for the high grade metamorphic rock were at 850-900 °C, at 0.95 (±0.10) GPa. For the structurally lower metasediments, >25 m away from the contact, peak conditions are lower at around ~700°C, at 0.95 (±0.10) GPa (Dubacq et al., 2019). With these constraints, Dubacq (2019) suggests these rocks recorded a retro-grade metamorphic path, as suggested

earlier by O'Beirne-Ryan et al. (1990). The cooling age of the metamorphic sole has been constrained to ~459 Ma, calculated by $^{40}Ar/^{39}Ar$ dating (Malo et al., 2008).

2.2.2 Mantle peridotite

The metamorphic sole and mantle peridotites are separated by a sharp boundary and a 20-40 m thick mylonitic contact zone (Dubacq et al., 2019; MacGregor & Basu, 1979; Whitehead et al., 1995). The contact zone comprises serpentinites with an ultra-mylonitic texture with its foliation sub-parallel to the contact. With increasing distance from the contact the mylonitic serpentinite gradually changes to a porphyroclastic peridotite. An exception to the rule is Mont. Olivine, located on the east side of Mont. Albert; here the peridotite is described to contain no to limited serpentine (MacGregor & Basu, 1979). The mantle is harzburgitic in nature (85%) and is interlayered by dunite channels (15%). Minor chromitite is present as foliation parallel lenses and pyroxenite is present as thin layers of dikelets (MacGregor & Basu, 1979). The peridotite contains orthopyroxene porphyroclasts and chromian-spinel. On a thin section scale, metamorphic olivine, amphibolite and clinopyroxene is found and can be linked to mylonite deformation (Dubacq et al., 2019).

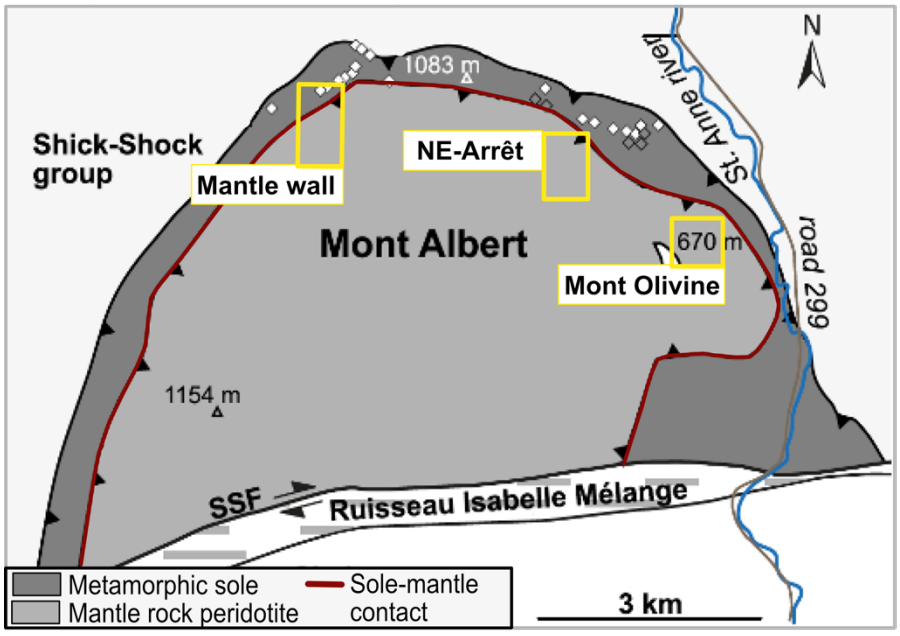

Figure 2 Lithology and basic structures of Mont Albert. Sampling locations for this study are indicated in yellow squares. Modified from Dubacq, 2018.

3. Methods

3.1 Sampling strategy

To research the chemical and structural effects of fluid infiltration into a mantle wedge, I collected a dense sample suite along a transect from the paleo-plate interface (-20 from contact) into structurally higher levels (60+ m of coherent section, and other complementary localities) of the mantle wedge. Most sampling was done on “Mantle wall”, which has a unique exposure of the mantle wedge. To fully represent the transition from slab to mantle, samples were taken from the metamorphic sole, contact zone, and deeper into the mantle rock roughly perpendicular to the foliation. Sample distribution at Mantle wall is shown as map view and strike-parallel view in Figure 3. Fifteen samples have been chosen to represent the slab-mantle transect, all shown in Table 1. To fairly compare samples that are most representative of Mantle Wall, only harzburgitic samples were collected. At Mantle wall, we distinguished different rock types based on changes in lithology; paying attention to changes in colour, mineralogy, textures/structures such as veining, compositional banding, boudins, porphyroclast content, and size. Based on these observations, we sub-divided Mantle Wall into four units and at least two samples were taken from every identified rock unit. The transect comprises collected samples roughly every ~5 m intervals of structural height (Figure 3a). After ~50 structural meters above the contact into mantle, the lithology became more consistent and the sampling density decreased (Table 1). The high sampling density in clear structural context distinguishes this study from previous research. Previous ophiolite analyses have indicated samples with >200 m distance from the contact show distinct geochemical signatures (Prigent, Guillot, Agard, & Ildefonse, 2018). This is why three samples were selected, 2 km east of Mantle wall, to represent the mantle rock further away from the contact, at 314 m and 850 m structural distance from their closest expressions of the contact (Figure 1b). Two additional samples were sampled from Mont Olivine, previously indicated by MacGregor & Basu (1979) to record the <10 % serpentinization of the peridotite. These samples can function as a proxy for the unserpentinized protolith.

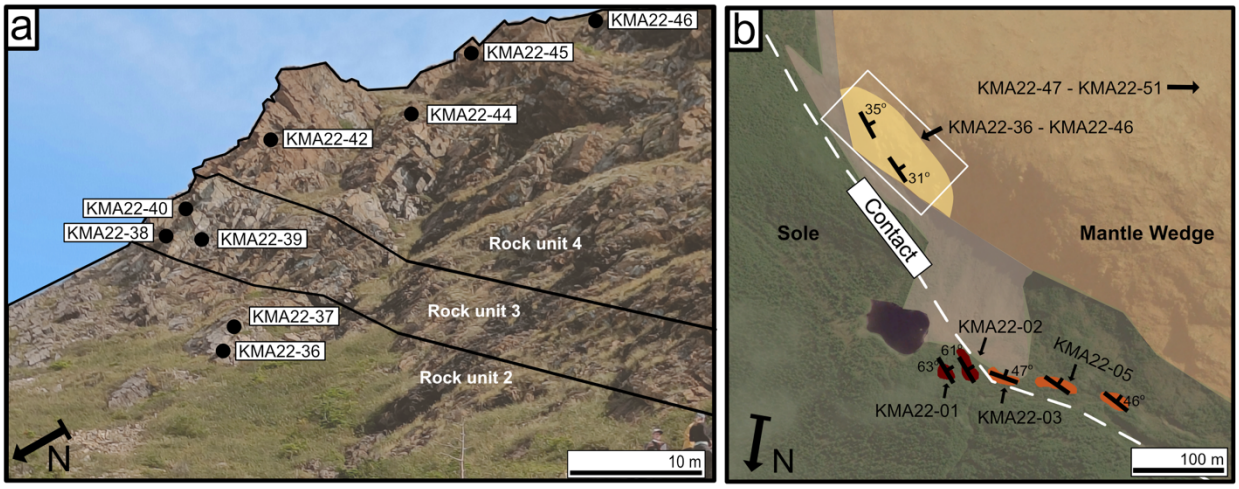

Figure 3 Location of sample selection. A) Roughly strike-parallel view of Mantle Wall showing south-dipping foliation and the exact sampling locations of Mantle Wall transect. Black lines indicate separation of rock units. B) GoogleEarth aerial view of Mantle Wall with geologic units, structural orientation and an approximation of the contact that runs between metamorphic sole and mantle wedge. Dark red is metamorphic sole, orange is contact mylonite and yellow is serpentinized peridotite. Green and grey is vegetation and gravel. Note: Sample KMA22-48 and KMA22-50 have been collected 2 km to the East outside of this view.

3.2 Analytical techniques

3.2.1 Optical and Electron microscopy

First order identification of mineralogy was done on Zeiss optical microscope and characterization of microstructural features Scanning Electron Microscope- Electron Dispersive Spectroscopy (EDS). With the EDS, I performed spot analyses on the main minerals of the sample and identified them by cross-referencing them against common EDS-spectra. Analytical conditions were set up at 20 kV and WD ~10 mm.

Sample	Type	Location	Distance from contact	Analytical techniques
			Contact is at 0m	
KMA22-01	Epidote amphibolite	Mantle wall	-20	Bulk rock chem.
KMA22-02	Garnet amphibolite		-15	Bulk rock chem.
KMA22-03	Ultra-myl. serpentinite	Mantle wall	16	Bulk rock chem., SEM
KMA22-05	Ultra-myl. serpentinite		24	
KMA22-36	Myl. serpentinite	Mantle wall	30	Bulk rock chem.
KMA22-37	Myl. serpentinite		31	Bulk rock chem.
KMA22-38	Myl. serpentinite		36	Bulk rock chem.
KMA22-39	Chromite layer		36	
KMA22-42	Myl. serpentinite		41	Bulk rock chem.
KMA22-44	Myl. serpentinite		46	Bulk rock chem.
KMA22-45	Myl. serpentinite		50	Bulk rock chem.
KMA22-46	Myl. serpentinite		60	Bulk rock chem.
KMA22-50	Porphyr. serpentinite		300	Bulk rock chem.
KMA22-47	Porphyr. serpentinite	NE-Arrêt	850	SEM, EMPA
KMA22-48	Porphyr. serpentinite		850	Bulk rock chem.
KMA22-12	Peridotite	Mont. Olivine	500	Bulk rock chem.
KMA20	Peridotite		500	EMPA

Table 1 Sample suite organized by their lithology and with increasing distance from the contact. All samples have been used for optical microscopy.

3.2.2 Bulk rock major element analysis via X-Ray Fluorescence (XRF)

Bulk rock major element analyses were performed to characterize host rock chemical heterogeneity, and to quantify first-order chemical effects of serpentinization. All fifteen samples from the sample suite were selected for major element analysis and represent the lithologic heterogeneity occurring across the mantle wedge hydration front. Major element analysis was performed by mixing the crushed rockpowder (80-mesh screen) with lithium borate. Major elements (SiO_2, TiO_2, Al_2O_3, Fe_2O_{3T}, MnO, MgO, CaO, Na_2O, K_2O, and P_2O5) were measured on a PANanalytical 2404 X-ray fluorescence vacuum spectrometer at Franklin and Marshall College, Pennsylvania, USA. Data were collected from the fused glass disks and presented as percent oxides. The Loss On Ignition (L.O.I.) was determined by comparing mass before and after baking at 950°C for 1.5 hours. A titration for ferrous/ferric iron determination was performed via the Reichen & Fahey (1962) method. Rock standards as used by Abbey (1983) and Govindaraju (1994) are used for quality control.

3.2.3 Bulk rock trace element analysis via laser ablation-inductively coupled plasma-mass spectrometry (LA-ICP-MS)

Bulk rock trace elements were analyzed in 15 samples across the mantle wedge hydration front in order to identify the trace-chemical fingerprints of metasomatism/serpentinization using the ThermoFischer Scientific Element 2 LA-ICP-MS at Utrecht University. Analytical precision allows quantification of extremely low concentration of elements, where concentrations often vary between 1 ppb - 100 ppm. Elements measured (Sc, V, Cr, Mn, Co, Ni, Cu, Zn, Ga, As, Rb, Sr, Y, Zr, Nb, Mo, Cs, Ba, La, Ce, Pr, Nd, Sm, Eu, Gd, Tb, Dy, Ho, Er, Yb, Lu, Hf, Ta, Pb, Th, U) were selected to include elements both very sensitive (LILE & LREE) and not sensitive (HREE) to fluid-facilitated alteration. This allowed us to interpret pre-, syn-, and post-subduction chemical signatures during the formation and alteration of the mantle rocks. The samples were cut into cm-sized blocks making sure surface alterations, weathering and late stage veins were not included in the block as best as possible. The samples were crushed and made into glass disks by melting it with lithium borate. In this process, contamination with tungsten is to be expected from the crushing. The beads were smashed to smaller pieces (<0.5 cm) to fit under the laser. Analytical conditions were 30 kV accelerating voltage and 120 mm beam size. For quality control the reference material N612 and BCR2G were analysed (at 26 kV) throughout the routine every six to nine measurements. All samples are measured three times to asses measurement reproducibility, after which values were averaged. Elements present in extremely low concentrations may yield erroneous measurements when approaching the detection limit. A

careful assessment of the dataset was made and evaluated on said errors, and some elements are excluded from further interpretation (e.g. Ta).

3.2.4 In-situ mineral composition via Electron Micro Probe Analyzer (EMPA)

In-situ major and minor elements (SiO_2, TiO_2, Al_2O_3, Fe_2O_{3T}, MnO, MgO, CaO, Na_2O, K_2O, and P_2O5) of olivine, orthopyroxene, clinopyroxene, and Cr-spinel were measured with the JEOL JXA-8530F Hyperprobe at Utrecht University. The elements were measured for a fully fresh peridotite (KMA20) and a partly serpentinized peridotite (KMA22-47). Quantitative microprobe analyses can determine how mineral chemistry changes during deformation and/or metasomatism and can determine the composition of the older, primary mineral. This technique allows for precise spot analysis perfect for reaction rims and smaller structures (e.g. exsolution lamellae). For example, I focused on core-rim zonation visible in BSE images to quantify changes in Cr-spinel chemistry during deformation; clinopyroxene-orthopyroxene pairs that were in textural equilibrium; and changes between olivine composition of large grains or fine-grained matrix.

Analytical conditions were 20 kV accelerating voltage, 15 nA probe current and 2 mm beam size. All minerals were measured 2-3 times, from which the average value was taken as final. Mineral chemistries were calculated based on ideal stoichiometry and the ferric and ferrous iron distribution was calculated using the charge balance equation (Droop, 1987; Schumacher, 1991).

4. Results

4.1 Outcrop to microscale: structural and petrologic observations

4.1.1 Mantle Wall

At Mantle Wall 80 meters of structural distance of both metamorphic sole and mantle rock is exposed. Sole rock expresses itself at the contact in a high grade amphibolite, consisting of amphibole, clinopyroxene, garnet, and minor plagioclase (Figure 5c). With increasing structural depth away from the contact, the rock comprises amphibole, epidote, and plagioclase. Foliation of sole rock is parallel to contact at 058/63 (strike/dip) and a lineation is exposed as 158/58 (azimuth/plunge). At Mantle Wall the exact contact between sole and mantle is covered by vegetation and gravel, but from other localities (e.g. NE-Arrêt) we know that the contact between metamorphic sole and mantle rock is a sharp, defined boundary (Figure 5a & 5b). Along the contact, serpentinite foliation strikes E-W, dipping 50-60° South, but become increasingly shallower where layers with +20 m of structural height are dipping 30-40° south. With structural height from the contact zone, the mantle rock succession shows an overall decrease in serpentine content, compositional banding becomes more diffuse/spread out and mylonitic texture transitions into porphyroclastic. To compare the mineral composition in the first 50 m of this structural transect is complicated by a strong serpentinization that has overprinted a lot of the original mineralogy. In all samples relicts of olivine, ortho- and clinopyroxene and Cr-spinel can be found, but to what extend they were present before fluid alteration remains suggestive. Observed changes in colour, degree of serpentinization, and fabric and shear structure characteristics justify sub-dividing Mantle Wall into four units of 5-10 m structural thickness as described in the following section. The different units of Mantle Wall are summarized in a stratigraphic column in Figure 4.

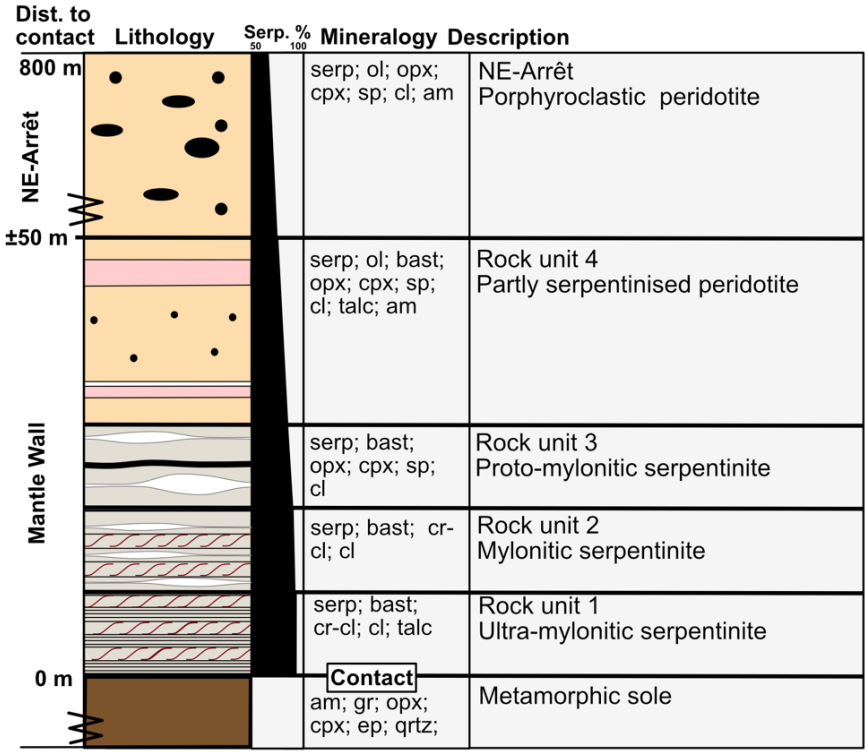

Figure 4 stratigraphic column of rock units found on Mantle Wall. Level of serpentinization and mineralogy is indicated.

4.1.1.1 Unit 1: contact zone/ultramylonitic serpentinite

4.1.1.1 Structural features

A 5-20 meter thick zone of fine-grained, ultra-mylonitic serpentinites forms the base of the Mantle Wall sequence. A NE-SW (45°) foliation dips 50° southeast and a lineation (133/50° (azimuth/ plunge)) is defined by serpentine minerals Orientation is similar to the structurally lower sole. Exposure of the full contact zone at Mantle Wall is bad, since most of the unit is covered in vegetation and is extremely weathered. The exposed rock shows mm-sized compositional banding with sharp, distinct boundaries, alternating between orange, pink/red and white serpentinite bands (Figure 5d). The bands show pinch and swell structures and shear structures indicating a top-to-the-North shear sense. In other localities, where exposure is better, the contact zone is estimated to be <10 m wide and the compositional banding contains other features, like phacoidal serpentine, micaceous surfaces in between layers, and foliation parallel chrysotile veining.

4.1.1.2 Micro-structural features

The ultra-mylonites consist mainly of a fine serpentine matrix (average 5-20 um) surrounding pseudomorphic bastites and Cr-spinel/chomechlorite porphyroclasts. The rocks have undergone near-complete serpentinization, where KMA22-03 reaches 100% serpentinization by volume and KMA22-05 reaches >90% by volume. On thin section scale, the samples are structured into sharp bands that are either colourless or brown in PPL (Figure 6 I). The colourless bands in PPL correspond to the red layers observed in the field and the brown bands in PPL correspond to the darkgrey layers. For KMA22-05, relict olivine (~3-5% by volume) occurs in the matrix as equant grains, ~5-20 um in size, with serpentinization localized to grain boundaries. Fluid altered pyroxene porphyroclasts are often unrecognizably serpentinized or have formed elongated pseudomorphic bastites (~200-1000 um). Bastites have foliation perpendicular fractures and 'tails' of finer grained serpentine within a serpentine layer. Sporadic, elongated, original orthopyroxene porphyroclasts (<1 % by volume) shows spaced cleavage that is kinked and/or bend. Black Cr-spinels porphyroclasts are partly or fully altered to a chrome-chlorite and show pull-apart structures, previously identified by Üner & Çakir (2011). For sample KMA22-03, the altered spinel grains have characteristic aureoles of chlorite (figure 6 Ib). Talc and chrysotile is present in veins (10-50 um) crosscutting the foliation (Figure 6 IIc). Magnetite is present within the serpentine grains as 1 um sized grains and dark-red hematite is concentrated in shear bands, fractures, and local serpentine networks. The shear bands that are observable in the field also appear on microlevel with the same shear senses and the serpentine mesh is deformed into a deformed ribbon texture.

Figure 5 a) Estimated contact (yellow line) between metamorphic sole and mantle rock on Mantle Wall foliation dipping South, b) Contact (yellow line) between metamorphic sole and mantle rock on NE-Arête, c) sole rock amphibolite containing quartz veins, d) rock unit 1 – mylonitic serpentinite e) iron rich shear bands in contact rock and rock unit 1, f) white lens in rock unit 2, g) chromite layer in rock unit 2, h) pink layering in rock unit 3 with foliation parallel chrysotile vein i) porphyroclastic peridotite, j) dunite channel between red lines, foliation in black lines, k) fresh peridotite from Mont Olivine

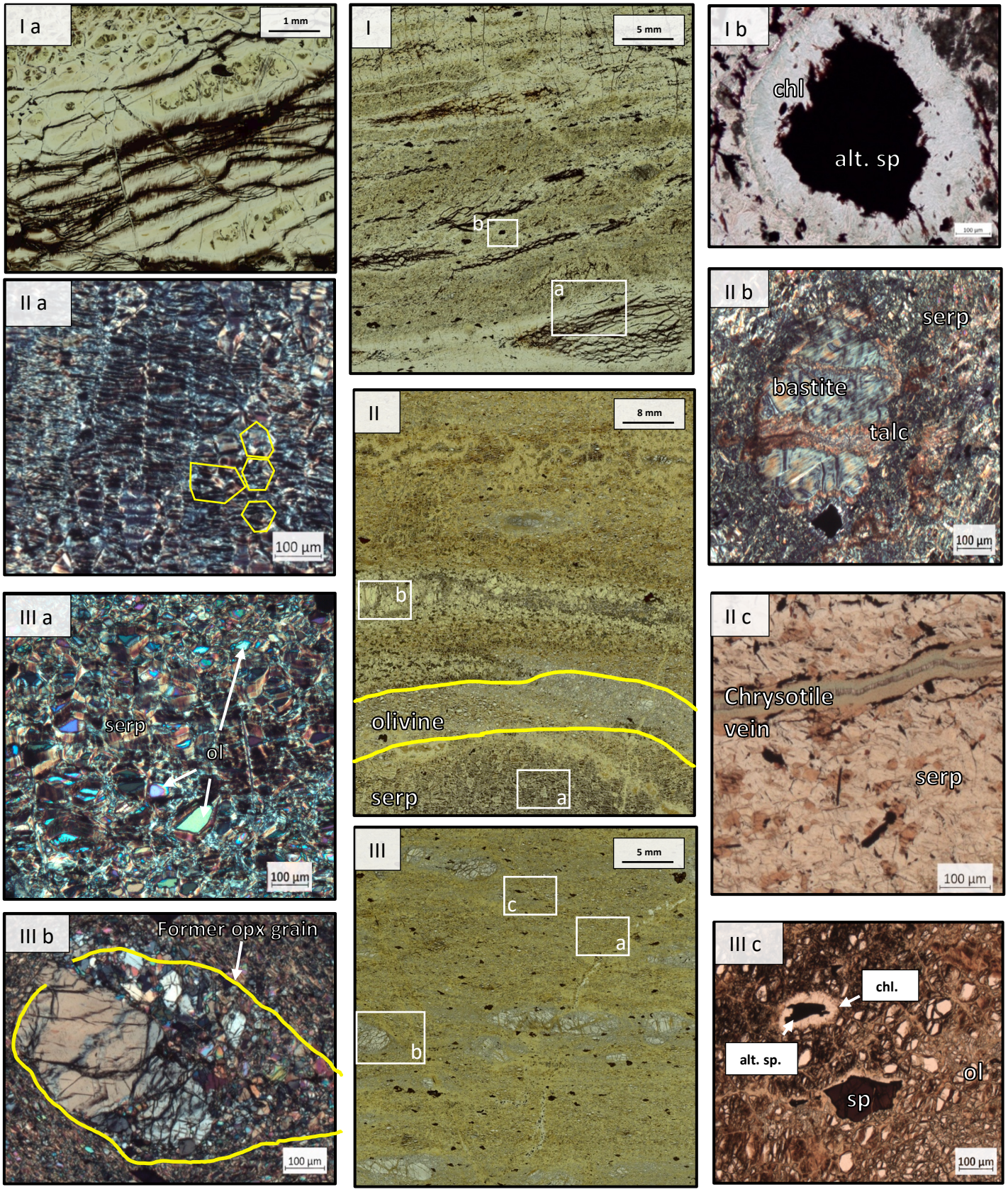

Figure 6 Microscopy of Mantle Wall rock units
I) PPL thin section of unit 1 - contact rock; Ia) Hematite network (PPL), Ib) altered chrome-chlorite spinel with chlorite aureole (PPL); II) PPL thin section of unit 4; IIa) ribbon serpentine mesh from pink banding with original ol grains in yellow (XPL); IIb) bastite with crosscutting talc veins (XPL); 11c) chrysotile vein in serpentine mesh (PPL);
III) PPL thin section NE-Arrêt porphyroclastic peridotite; IIIa) Relict olivine grains with serpentine near grain boundary (XPL); IIIb) former opx grains, replaced with coarse grained ol and opx (XPL); IIIc) unaltered and altered spinel grains in a olivine/serpentine mesh (PPL) Serpentine is heavily affected by browning, which previously observed and defined by Albers et al. (2020) as a late stage fluid alteration.

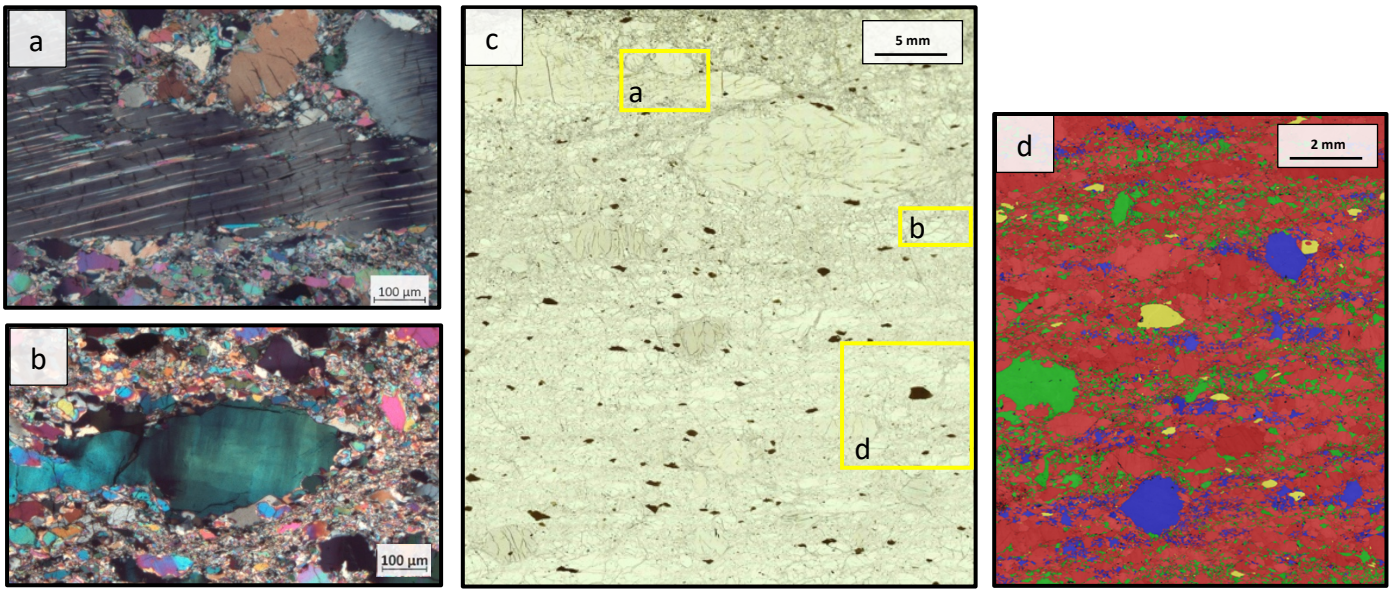

Figure 7 Microscopy from Mont Olivine a) orthopyroxene with bending in clinopyroxene exsolution lamellae (XPL) b) undulose extinction in original olivine (XPL) c) PPL image of thin section of peridotite d) EBSD map of section of thin section

4.1.1.2 Unit 2: mylonitic serpentinite

4.1.1.2 structural features

Following the contact zone, unit 2 comprises a ~5 m unit of fine grained mylonitic serpentinites, with an E-W (65°) foliation dipping 40° south. A lineation (151/10° (azimuth/plunge)) is defined by serpentine minerals. Unit 2 consists of alternating red, darkgrey and white compositional banding similar to unit 1 (Figure 5e). The white layers contain pinch and swell structures, forming white serpentine lenses throughout anastomosing orangebrown bands of serpentine. In contrast to unit 1, bands are thicker (1 mm – 1 cm) and are structured into white layers that contain red shear bands indicating top to North shear sense. Between the compositional layers, sub-milimeter micaceous layers have formed. Unlike unit 1, sub-milimeter sized black porphyroclasts can be observed in unit 2; possibly due to better exposure. Similar to unit 1, foliation parallel chrysotile veins are observed, with characteristic fibers perpendicular to the foliation.

4.1.1.2 micro-structural features

Similar to unit 1, unit 2 comprises a serpentine matrix (10-50 um) containing bastites, equant primary olivine, and Cr-spinel/chomechlorite porphyroclasts. Cr-spinel occurs as sightly elongated grains and have chlorite aureoles, that seem unrelated to distance to contact or level of serpentinization. Samples are near-complete serpentinized (>95% by volume), similar to unit 1. Shear structures are less prominent, but still visible in hematite rich bands and as brittle fractures

in the serpentine mesh. The serpentine mesh consists of larger grains (average 30-50 um) compared to unit 1.

4.1.1.3 Unit 3: Proto-mylonitic serpentinite

4.1.1.3 structural features

Unit 3 comprises a ~5 m unit of porphyroclastic proto-mylonites. Orientation is similar to unit 2. This unit has a distinctive grey/whiteish weathered colour and contains larger porphyroclasts (0.1-0.5 cm) compared to unit 2. Compared to earlier rock units, this rock has a coarser grained sugary texture and observable olivine minerals, indicating a lesser degree of serpentinization. This unit comprises cm-scale, white, fine grained serpentinite lenses (Figure 5F). In contrast to rock unit 1 and 2, this unit contains mm-scale black chromite layers and pink serpentinite layers (2-3 cm) along foliation spread intermittently throughout the unit (Figure 5g).

4.1.1.3 micro-structural features

Similar to rock unit 1 and 2, rock unit 3 has undergone 90-95% serpentinization. On thin section scale, the sample is still structured in darker iron rich and transparent bands, but the distinction between banding is more diffuse. Unlike previous units, primary equant olivine (10-20 um) is preferentially located in foliation parallel layers encased by serpentine layers, rather than spread throughout the serpentine matrix. Similar to previous units, the presence of bastites and Cr-spinel is common in Unit 3 textures. However, the Cr-spinel lack the characteristic chlorite aureoles in this unit, possibly due to sampling bias.

4.1.1.4 Unit 4: porphyroclastic peridotite

4.1.1.4 structural features

Rock unit 4 is characterized by a typical brown/orange colour in the field. The colourful compositional banding is no longer present, except for the presence of pink layers (1-10 cm) that are spaced >1 m from each other (Figure 5h). The pink layering has diffuse boundaries and sometimes have flame-like edges into the neighbouring layer. Compared to previous units, the pyroxene and spinel porphyroclasts have increased in size (0.5-0.8 cm) (Figure 5j). Similar to unit 2, there are sub-millimetre micaceous layers in between the brown and pinkish layers and additional booklets of micaceous material (~3 cm) are present on the surface of the outcrop.

4.1.1.4 micro-structural features

Unlike the previous units, Unit 4 has less penetrative serpentinization as shown by ~40% relict olivine, present as equant slightly elongated grains (10-50 um) spread homogeneously, forming a serpentine-olivine matrix. The foliation parallel pink bands, observed in the field, consist of iron rich, ribbon textured serpentine, where original olivine grain boundaries are still visible through the texture (Figure 6 II & IIa). This ribbon-textured serpentine layer is bound by a layer of olivine on both sides. In contrast to previous rock units, iron is no longer concentrated in dark vein networks or shear bands. Original and partly serpentinized orthopyroxene porphyroclasts (200-1000 um) are present throughout the olivine-serpentine matrix. They are less elongated compared to the bastite in previous units and no longer have fine grained 'tails'. Instead the porphyroclasts are surrounded by a coarse grained olivine; coarser along grain boundary (50 um), fining towards the matrix (10 um). Some orthopyroxene grains are partly replaced by a coarse grained olivine and orthopyroxene (20-50 um) (Figure 6 IIIb). In addition to the black Cr-spinels in the previous units, Cr-spinels grains (10-90 um) are also a rich brown and are homogeneously spread throughout the section. Similar to the previous rock units porphyroclasts exhibit evidence for fluid alteration, e.g. chlorite rims and cross cutting talc veining (Figure 6 IIb). Singular grains of amphibole (<0.5% by volume) are present as equant porphyroblasts (100 um).

4.1.2 NE-Arrêt

4.1.2.1 structural features

Unit 4 is found 300-800 m from the contact and is a typical porphyroclastic peridotite (Figure 5j). It is best outcropped 2 km East of Mantle Wall and has an average 290/90 S (strike/dip) foliation and 15/305 (plunge/azimuth) lineation defined by spinel grains. The red/pink compositional banding and shear bands are no longer observable. A foliation is still present in the alignment of elongated serpentine and spinel grains. At times, the harzburgitic layers are disrupted by foliation parallel channels that are devoid of porphyroclasts and are considered to represent dunite channels (Figure 5j). Similar to unit 4, large chunky patches of phyllosilicates sit on the surface of the rock. Porphyroclasts are bigger (1 cm) and are well-rounded as opposed to elongated. Pyroxene porphyroclasts and/or pseudomorphic bastite show a characteristic brittle fracture pattern, where only the clasts contain cm-scale fracture gashes perpendicular to the foliation.

4.1.2.2 micro-structural features

Samples from NE-Arrêt are 40-50 % serpentinized and are texturally and mineralogically very similar to the structurally highest Mantle Wall sample (KMA22-46). Matrix comprises of coarse olivine grains (20-50 um) rimmed by extremly fine grained serpentine (<1 um) around the grain boundaries (Figure 6 IIIa). Olivine grains form part of a larger original clasts (100-200 um), visible by simultaneously extinction. In contrast to previous units, pyroxene porphyroclasts and bastites form rounded grains (500-1000 um) with parallel spaced cleavage. Porphyroclasts of orthopyroxene are broken up by serpentine networks, but relict material is still observable. Similar to previous units, brown to black Cr-spinel grains have a heavily fractured internal structure and range from unaltered to completely altered into chrome-chlorite with chlorite aureoles (Figure 6 IIIc). Especially sample KMA22-47 is heavily altered by fluids, exhibited by the presence of talc veins crosscutting foliation and cutting through porphyroclasts

4.1.3 Mont Olivine

4.1.3.1 structural features

In contrast to a heavily serpentinized Mont Albert, Mont Olivine shows a significant exposure of unserpentinized peridotite (Figure 5k). Exposure of the first 100 structural meters of the peridotite is bad and the exact contact is obstructed by vegetation. On top of Mont Olivine foliation is 130/80 S (strike/dip) and lineation is defined by serpentine grains 40/135 (plunge/azimuth). Exposed rock is orange-brown with a green sheen and has a distinct weathering pattern forming a striped surface. The rock is coarse grained with a sugary texture and samples contain black mm-cm sized grains of pyroxene. Foliation crosscutting fractures indicate brittle deformation. On top of Mont Olivine mixed types of shear bands are found indicating both Top-to-North and Top-to-South shear sense. Similar to unit 4 and NE-Arête, patches of micaceous booklets are found on the surface of pieces of float.

4.1.3.2 microstructural features

Mont Olivine samples are identified as a homogeneous harzburgitic lherzolite (Figure 8). Fresh peridotites consists of a fine grained matrix (1-10 um) that consists primarily of irregularly shaped and interwoven olivine, orthopyroxene, and clinopyroxene. The matrix contains larger clasts of olivine, ortho- and clinopyroxene and Cr-spinel. Olivine grains (50-200 um) exhibit a strong shape preferred orientation, with long axes defining a clear stretching lineation. Grains are spread homogeneously throughout the matrix and show undulous extinction (Figure 7b). The

orthopyroxene porphyroclasts (100-1000 um) show the same shape preferred orientation as the olivine and clasts are often surrounded by a rim of very fine grained matrix (1 um). Clasts contain bend clinopyroxene exsolution lamellae and inclusions of clinopyroxene and Cr-spinel (Figure 7 a). The Cr-spinel (20-100 um) comprises 1.4 % of the total volume, are euhedrally shaped and are often aligned comprising a lineation. In contrast to the serpentinized samples, the unaltered Cr-spinel is always brown and shows no internal fracturing. The grain boundaries between matrix and porphyroclasts/porphyroblasts are bulging and show some phase mixing. The porphyroclasts/-blasts are sided with tails of matrix material preferentially containing porphyroclasts/-blasts material; the porphyroclasts/-blasts material seems to extend into the matrix in foliation parallel bands (Figure 7d).

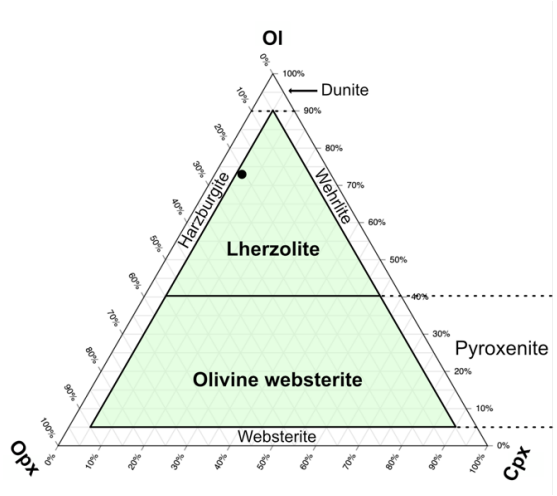

Figure 8 Ternary diagram for sample KMA20, which is a representative for fresh peridotite. Black dot represents the composition of peridotite.

4.2 Geochemical results

4.2.1 Major elements (bulk rock)

Metamorphic sole

Two samples from the metamorphic sole contain high 9.00-13.00 wt% CaO, 15.00 wt% FeO_T, low 9.00±1.00 wt% MgO, and 13.00±1.00 wt% Al_2O_3. Iron is present as 9.00±0.90 wt% FeO and 5.00±1.00 wt% Fe_2O_3. The structurally lower epidote-amphibolite contains lower concentrations of 44.00 wt% SiO_2, and 0.69 wt% TiO_2 compared to the structurally higher garnet-amphibolite that contains higher concentrations of 51.00 wt% SiO_2 and 1.20 wt% TiO_2. Concentrations of L.O.I. decrease towards the contact with 1.92 wt% for the epidote-amphibolite and 2.40 wt% for the garnet-amphibolite (Figure 9).

Mantle rock

At Mantle Wall, NE Arrêt, and Mont Olivine concentrations of anhydrous ratios MgO/SiO_2 and Al_2O_3/SiO_2 show a broad range. Figure 10 shows all datapoints fall on the terrestrial array; which shows the melting evolution from a depleted mantle. Mont Olivine peridotites (n=2) have 0.04 ±0.02 wt% Al_2O_3/SiO_2 and 0.95±0.01 wt% MgO/SiO_2. Serpentinized Mantle Wall samples with <60 m structural height (n=9) range between 0.03-0.07 wt% Al_2O_3/SiO_2, increasing the ratio with 0.10 ±0.10 for every 5 m away from the contact, and range from 0.93-1.01 wt% MgO/SiO_2 with no clear structural correlation. Partly serpentinized NE-Arrêt samples with >300 m of structural height from the contact contain 0.020±0.006 wt% Al_2O_3/SiO_2 and 1.03+0.04 wt% MgO/SiO_2 (n=3). Mont Olivine samples have a relatively low Mg# of 0.83±0.00, compared to Mantle Wall samples which have a Mg# of 0.96±0.01 for samples with <60 m of structural height and Mg# of 0.93±0.01 for samples with >300 m of structural height. Concentrations range from 0.12 – 1.98 wt% CaO with no clear trend with sampling location or structural distance from the contact. All mantle samples (n=15) contain low 0.02±0.02 wt% TiO. Cr and Ni concentrations range from 2400-3500 ppm and 2312-2699 ppm with no structural correlations.

Low concentrations of 1.07-1.29 wt% Fe_2O_3 for Mont Olivine samples increase sharply to 5.40-8.49 wt% Fe_2O_3 for the serpentinized samples. Ferric iron content is highest closer to the contact, where the level of serpentinization is also highest. When normalized to MgO, the ferric iron concentrations are level throughout the transect (see Figure 9). Mont Olivine peridotites have low 0.81-0.84 wt% L.O.I., while all serpentinized Mont Albert samples range from 12-14 wt%, consistent with observed, near-penetrative serpentinization (Figure 9). Concentrations of SiO_2, MgO, and Al_2O_3 vary only slightly with L.O.I.; having a range of 2-5 wt% for all oxides. This

indicates no to limited major element mobility during serpentinization (see *supplementary Figure 1*).

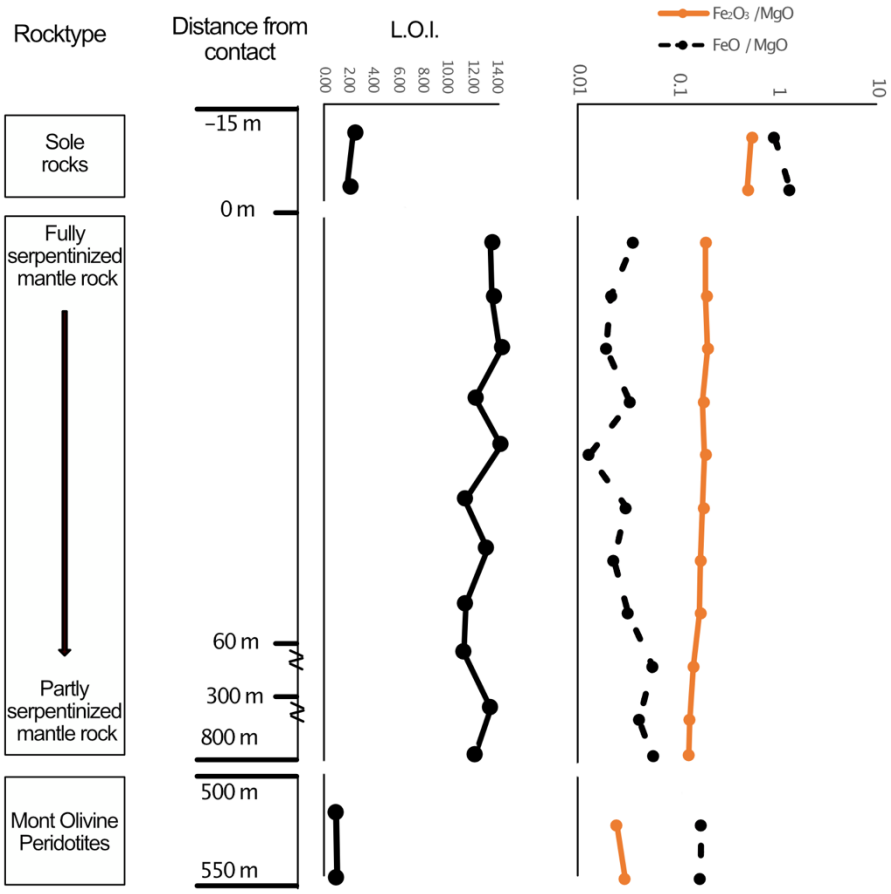

Figure 9 Levels of L.O.I. and Ferrous and Ferric iron content normalized to MgO. Datapoints are set against their distance relative to the contact.

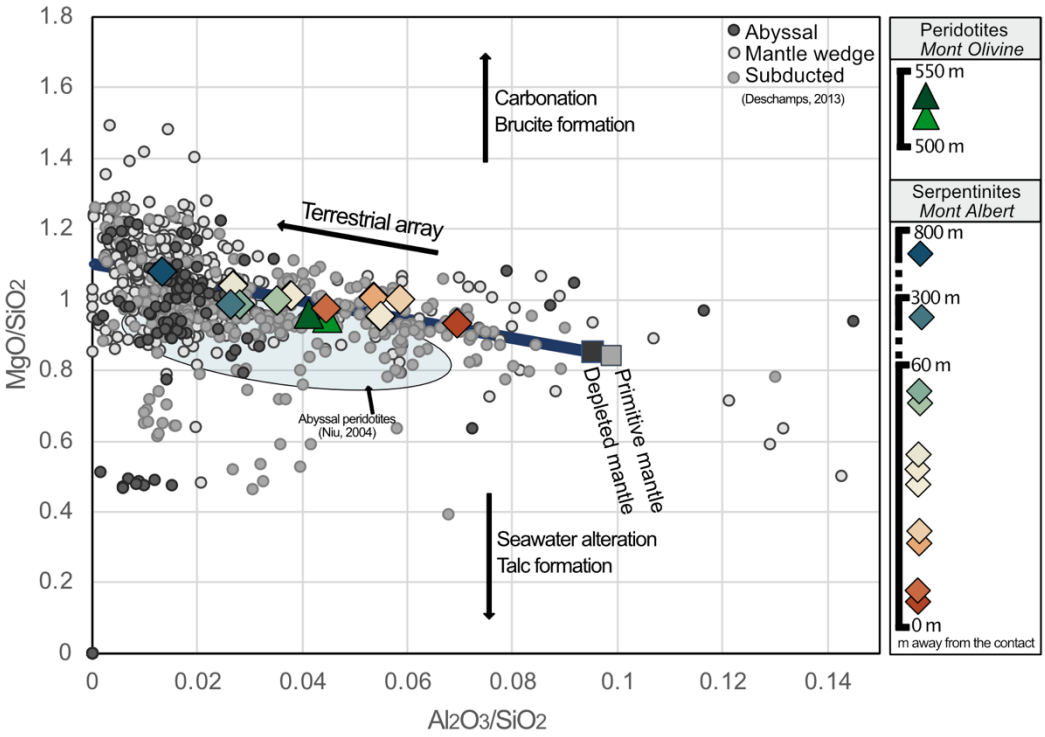

Figure 10 Ratios of MgO/SiO2 and Al2O3/SiO2 throughout the sample transect. Red squares are the fully serpentinized samples closest to the contact transitioning into blue which represent the partly serpentinized samples. Fresh peridotite is represented as triangles in green. Global dataset collection from Deschamps et al. (2013) are shown in grey circles as comparison. The blue bubble under the terrestrial array is defined for abyssal peridotites by (Niu, 2004). The dark blue line indicates the 'terrestrial array', which represents Earth's melting array from depleted mantle (Jagoutz et al., 1979). Moving up or down from the terrestrial array often indicates carbonation or seawater alteration respectively. Depleted and primitive mantle values are taken from McDonough & Sun (1995).

Table 2 Bulk rock major and trace element concentrations

Lithology	Amphibolite		Serpentinite											Peridotite	
Location	Mantle wall		Mantle wall									NE-border		Mont Olivine	
Structural distance from the contact	-20	-15	15	24	30	31	36	41	46	50	60	310	850	500	550
Sample	KMA22-01	KMA22-02	KMA22-03	KMA22-05	KMA22-36	KMA22-37	KMA22-38	KMA22-42 L1	KMA22-44	KMA22-45	KMA22-46	KMA22-50	KMA22-48	KMA22-12	KMA20
Major wt%															
SiO2	43.94	50.98	43.57	43.84	43.17	43.12	43.87	44.10	43.35	43.87	44.33	43.21	44.64	44.58	44.24
TiO2	0.69	1.18	0.09	0.02	0.03	0.03	0.02	0.02	0.01	0.01	0.01	0.00	0.01	0.01	0.01
Al2O3	14.63	12.32	3.02	1.95	2.31	2.53	1.65	2.42	1.16	1.54	1.25	0.57	1.18	2.00	1.82
Fe2O3T	15.09	14.99	9.24	9.06	9.45	9.26	8.82	8.82	8.72	8.80	8.90	8.22	8.71	8.80	8.88
MnO	0.24	0.21	0.13	0.12	0.13	0.13	0.12	0.13	0.12	0.12	0.13	0.11	0.12	0.12	0.13
MgO	10.37	8.38	40.64	42.65	43.53	43.19	44.34	42.02	45.21	43.76	43.72	46.56	44.05	42.26	42.51
CaO	13.44	9.27	1.98	1.46	0.24	0.76	0.12	1.78	0.33	1.01	0.94	0.33	0.57	1.79	1.93
Na2O	1.53	1.54	0.14	0.08	0.05	0.08	0.11	0.20	0.13	0.08	0.07	0.06	0.07	0.07	0.06
K2O	0.40	0.76	0.03	0.01	0.00	0.00	0.01	0.02	0.01	0.00	0.00	0.00	0.00	0.01	0.00
P2O5	0.06	0.12	0.01	0.00	0.00	0.00	0.01	0.01	0.01	0.00	0.00	0.00	0.00	0.00	0.00
Total	**100.39**	**99.75**	**98.86**	**99.19**	**98.92**	**99.11**	**99.06**	**99.52**	**99.04**	**99.20**	**99.35**	**99.06**	**99.36**	**99.64**	**99.59**
LOI	2.40	1.92	13.44	13.59	14.28	12.11	14.13	11.19	12.92	11.19	11.08	13.38	12.07	0.84	0.81
FeO	8.71	9.88	1.46	0.95	0.86	1.46	0.60	1.29	1.06	1.42	2.46	1.96	2.98	6.96	6.83
Fe2O3	5.41	4.01	7.62	8.00	8.49	7.64	8.15	7.39	7.54	7.22	6.17	6.04	5.40	1.07	1.29
Mg#	0.48	0.40	0.96	0.97	0.98	0.96	0.98	0.96	0.97	0.96	0.93	0.95	0.92	0.82	0.83
Al2O3/SiO2	0.333	0.242	0.069	0.044	0.054	0.059	0.038	0.055	0.027	0.035	0.028	0.026	0.013	0.045	0.041
MgO/SiO2	0.24	0.16	0.93	0.97	1.01	1.00	1.01	0.95	1.04	1.00	0.99	0.99	1.08	0.95	0.96
Minor / Trace (ppm)															
Sc	67.16	57.98	20.35	15.78	18.02	18.41	12.25	15.24	12.04	14.55	14.96	7.59	10.68	17.50	15.84
V	382.22	379.50	77.00	48.99	41.41	52.74	44.70	58.94	46.89	44.16	55.01	22.37	29.41	58.19	55.50
Cr	311.36	187.70	3585.82	2966.10	2953.32	3229.33	3053.48	2850.79	3194.27	3109.75	3263.87	2461.03	2495.90	3142.94	3030.21
Mn	1863.65	1649.84	863.00	933.32	1034.63	1020.76	932.27	1012.97	972.52	941.94	947.22	774.63	900.19	998.16	966.82
Co	150.59	74.50	126.51	126.81	157.87	133.97	127.19	127.98	137.71	120.83	268.24	125.47	151.58	138.67	134.84
Ni	136.80	105.27	2477.91	2377.60	2312.38	2396.27	2568.81	2345.81	2699.47	2363.88	2409.20	2424.78	2562.26	2328.20	2270.31
Cu	101.70	72.81	20.31	17.46	17.55	13.44	15.69	19.67	13.23	9.39	37.63	4.52	11.24	22.89	20.73
Zn	111.95	128.29	67.45	70.18	66.00	74.81	58.60	67.58	71.69	66.65	72.36	64.80	66.72	67.76	65.31
Ga	16.86	16.22	3.53	2.36	2.26	2.66	1.92	2.30	2.04	2.49	1.85	1.68	1.26	1.87	1.39
As	1.91	1.67	2.30	2.14	2.27	2.23	2.01	<1.59	<2.2	<2	2.48	<1.8	1.66	2.21	2.12
Rb	5.76	7.59	0.72	0.48	0.30	0.55	0.32	0.46	0.42	0.47	0.58	0.34	0.64	0.51	0.43
Sr	99.81	36.99	3.29	2.68	3.04	2.20	1.81	3.22	1.62	2.09	<0.49	<0.56	0.76	0.52	<0.50
Y	20.35	36.23	1.72	0.78	1.40	1.61	0.59	1.16	0.27	0.74	0.46	0.13	0.17	0.49	0.50
Zr	22.07	333.46	1.85	1.51	2.58	2.36	2.08	2.05	1.22	1.48	1.29	1.29	1.80	1.60	1.35
Nb	0.91	9.24	0.07	0.03	0.04	0.08	0.07	0.06	0.04	0.04	0.07	0.04	0.05	0.08	0.04
Mo	1.37	1.39	1.55	1.28	1.34	1.10	1.32	1.72	1.37	1.27	1.34	1.16	1.11	1.49	1.02
Cs	0.18	0.36	0.03	<0.03	<0.03	<0.03	0.07	0.10	0.04	0.03	0.03	<0.03	<0.03	0.03	0.03
Ba	25.60	55.05	4.33	3.62	3.89	2.96	2.56	3.51	3.98	3.28	2.89	2.42	2.31	2.50	2.81
La	1.13	22.25	0.09	0.05	<0.03	0.05	0.05	0.06	0.07	0.04	0.08	0.03	0.05	0.09	0.04
Ce	3.46	46.32	0.13	0.06	0.02	0.05	0.14	0.05	0.06	0.02	0.03	0.05	0.05	0.06	0.03
Pr	0.50	5.56	0.03	0.03	0.01	0.02	<0.02	0.02	0.01	<0.015	<0.02	<0.01	<0.02	0.02	<0.02
Nd	3.26	22.33	0.11	0.05	0.09	<0.09	0.12	0.11	0.08	<0.08	0.02	<0.09	0.11	0.08	0.06
Sm	1.35	4.92	0.09	0.01	0.06	<0.07	<0.058	0.07	0.06	0.04	0.04	0.09	0.07	0.06	0.04
Eu151	0.59	1.27	0.10	<0.08	<0.11	<0.11	<0.12	0.17	<0.133	<0.14	<0.1	<0.12	<0.13	<0.10	<0.12
Eu153	0.53	1.35	0.13	<0.09	<0.14	<0.14	<0.15	<0.15	<0.66	<0.142	<0.11	<0.13	<0.15	0.12	<0.15
Gd	2.35	5.00	0.21	<0.15	0.19	0.18	0.21	<0.20	<0.21	<0.22	0.25	<0.13	<0.13	0.15	<0.12
Tb	0.43	0.81	0.05	0.03	0.05	0.04	<0.03	0.03	<0.13	<0.027	0.03	<0.03	0.02	<0.03	<0.24
Dy	3.41	5.97	0.29	0.17	0.19	0.22	0.10	0.22	<0.07	0.09	0.11	0.01	0.09	0.08	<0.07
Ho	0.71	1.29	0.07	0.03	0.06	0.06	0.03	0.03	0.02	0.03	0.02	0.02	0.02	0.03	0.03
Er	2.32	3.99	0.21	0.08	0.14	0.18	0.09	0.10	0.10	0.10	0.11	0.05	0.06	0.08	0.08
Yb	2.46	4.24	0.26	0.15	0.17	0.23	0.11	0.18	0.13	0.09	0.08	0.02	0.05	0.09	0.08
Lu	0.38	0.63	0.04	0.02	0.03	0.03	0.02	0.04	0.02	0.02	0.02	0.05	0.01	0.02	0.02
Hf	0.71	8.30	0.10	0.08	0.13	0.09	0.09	0.05	<0.07	0.11	0.09	0.09	0.10	0.09	0.10
Ta	0.51	0.99	0.50	0.45	0.39	0.48	0.44	0.40	0.50	0.49	0.50	0.44	0.48	0.52	0.51
Pb	0.89	0.70	0.15	0.41	0.52	0.19	0.20	0.15	0.18	0.15	0.18	0.23	0.14	0.13	0.13
Th	0.14	5.13	0.01	0.01	0.01	0.02	0.01	0.01	0.02	0.00	0.01	0.01	0.00	0.01	0.01
U	0.12	0.44	0.02	0.01	0.01	0.01	0.01	0.16	0.02	0.01	0.01	0.02	0.02	0.56	0.01
Eu/Eu* (normalised)	0.91	0.83		3.02										3.83	
Ce*/Ce (normalised)	0.64	2.18		0.20	0.08	0.10	0.27	0.09	0.09	0.06	0.05	0.11	0.11	0.10	0.07
La/Yb (normalised)	0.46	5.25	0.25	0.20	-	0.14	0.27	0.22	0.34	0.28	0.66	0.72	1.32	0.67	0.32
La/Sm (normalised)	0.84	4.53	1.11	3.21	-	-	-	0.83	1.03	0.90	2.08	0.76	0.344086022	1.614942529	1.057142857
Sm/Yb (normalised)	0.55	1.16	0.33	0.09	0.34	-	-	0.38	0.49	0.45	0.46	1.39	5.64	0.61	0.45

4.2.2 Trace elements (bulk rock)

4.2.2.1 Metamorphic sole

Generally, REE concentrations are flat and enriched relative to C1 chondrite. Concentrations of HREEs for the garnet- and epidote- amphibolite are similar. Concentrations of LREE deviate between the two samples where the garnet amphibolite forms a negative slope from LREE to HREE, in contrast to the epidote amphibolite which forms a positive slope. Concentrations of Nb and Zr are variable between the two samples with Zr_{epi}= 22 and Zr_{gar}=333.46, and Nb_{epi}= 0.92 and Nb_{gar}=9.24. Concentrations of Ti are high with Ti_{epi}= 4486.92 and Ti_{gar}=8501.34. Additional relevant element ratios are Zr/Y_{epi}=1.08 and Zr/Y_{gar}=9.20; V/Ti_{epi}=0.085 and V/Ti_{gar}=0.044.

4.2.2.2 Mantle rock

Trace element patterns are consistent throughout the sample suit and have element enrichments typical for serpentinite. Some variations exist for REE concentration that can be correlated to their structural distance from the contact.

REE

Correlations between REEs, major element MgO, and HFSEs indicate which elements have been affected by a similar mobilizing process (magmatic or fluid assisted). These correlations are made between elements with similar incompatibility, to ensure their behaviour is also similar during mobilizing processes (Niu, 2004). Previous research by Niu (2004) established that between trace elements a correlation with a value of R>0.3 can be considered as relevant and thus means both elements are mobilized by the same process. All relevant correlations can be found as *supplementary table 1*. For correlations between trace elements and MgO, a value of R< -0.3 is considered relevant.

Excellent negative correlations (R<-0.6) exist between MgO and HREE (Tb, Dy, Ho, Lu, Er, Yb). In contrast MgO and most LREE (Ce, Nd, Pr) form poor correlations of R>-0.3, with the exception of La which forms a correlation of R=-0.6. Concentrations of HREE (Tb, Dy, Ho, Lu, Er, Yb) and the fluid-immobile HFSE (Ti, Zr, Hf, Ta, Nb) correlate well with 0.4< R <0.9. Good correlations exist between La and Ce (LREE), HREE and HFSE with overall R>0.3 and bad correlations exist between Nd and Pr (LREE) and HFSE with R<0.15.

Concentrations of REE, normalized to C1 chondrite, plot slightly below the DM trendline (Figure 11). Both samples from NE-Arête contain concentrations too low to meet the detection limit. Other samples show a decrease in HREE concentrations with structural distance to the contact, where e.g. Yb_N= 1.2±0.2 (n=4) for samples <20 m of structural height and Yb_N=0.2 ±0.1$_N$

(n=4) for samples with >300 m of structural height. Figure 11 shows samples with a <20 m structural distance from the contact plot on the 5% melting array line, while samples >300 m from the contact plot closer to the 15% melting array line. In contrast to the HREE, concentrations of LREE's do not show correlation between concentration and structural distance from the contact. In Figure 11, LREE concentrations plot slightly higher than the typical melting array would, especially for samples furthest away from the contact. The positive slope from LREE to HREE is shown by e.g. La/Yb and ranges between 0.14-0.34 for samples <50 m of structural height and increases sharply to 0.65 – 1.31 for samples with >60 m of structural height.

FME

Trace elements, normalized to primitive mantle, generally plot slightly below depleted mantle, as defined by McDonough & Sun (1995) and multi-element pattern are slightly U-shaped compared to DM and GLOSS II (Figure 12). The multi-element diagram shows strong enrichments in U and Pb and concentrations of Cs, Rb, Ba, and La are slightly elevated relative to neighbouring elements and depleted mantle. Data also shows a small positive anomaly for Eu $(Eu/Eu^*)_N$ = ~3 (n=3) and a small Ce depletion $(Ce/Ce^*)_N$=~0.12 n=10). Concentrations of As are relatively high compared to mantle values with As=2.157 ppm ±0.22 (n=9). Concentrations of Ti are highly variable ranging between 37-388 ppm; concentrations are overall high at the contact and decrease with structural distance. What is surprising is that the fresh peridotites (green in figure 12) are as enriched in FME as the serpentinites compared to depleted MORB mantle. Most LILE or FME (e.g. Cs and Pb) have similar composition for all samples in the structural transect and show no clear correlation between level of serpentinization and FME content. Very limited distinction exists between some FMEs (e.g. Rb, Ba, Sr) of the serpentinized samples and the fresh peridotite, where concentration is increased with max 20% for the serpentinites (see Figure 18b).

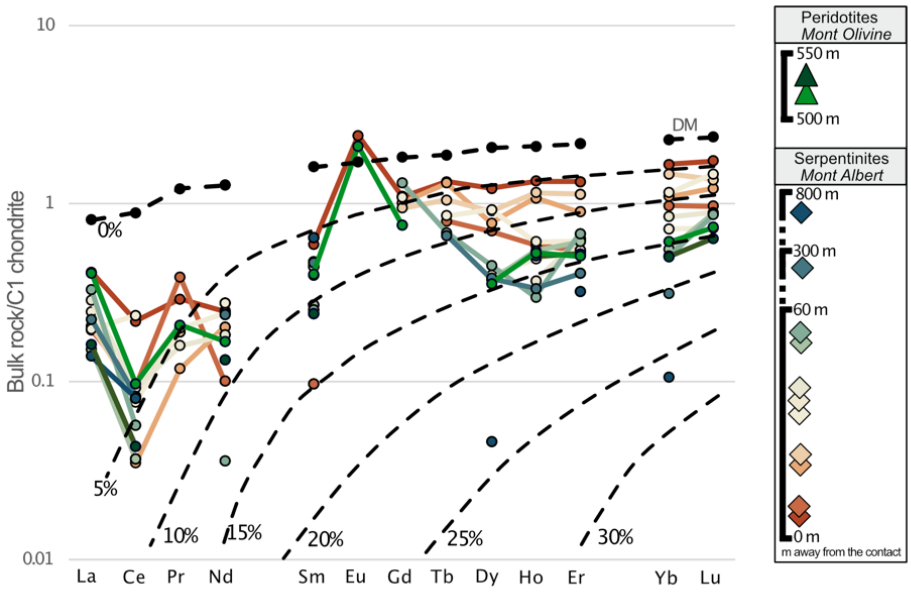

Figure 12 REE pattern together with the melting trends estimated from Niu (2004). They represent the melting array from a depleted MORB mantle, assuming fractional melting. DM and C1 chondrite values are taken from Mcdonough and Sun (1995)

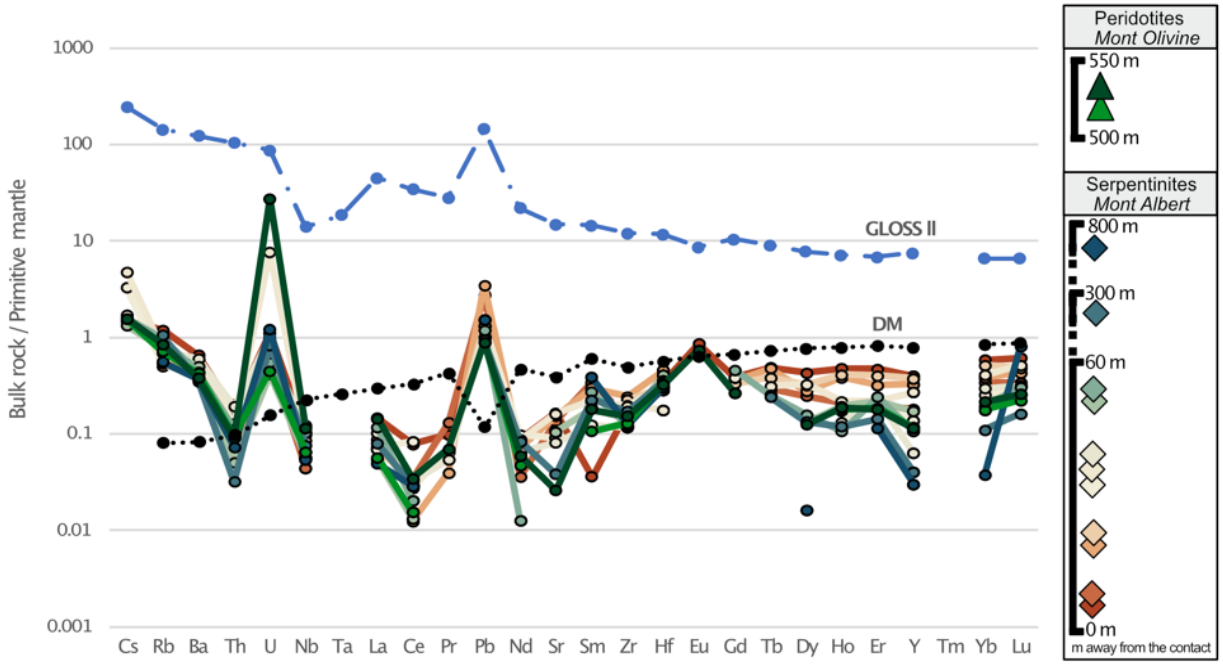

Figure 11 multi-element spider diagram with selected elements like Deschamps (2013). Gloss is taken from has been plotted for comparison to determine on sediment influx. Primitive mantle values and depleted mantle (DM) is taken from McDonough & Sun (1995).

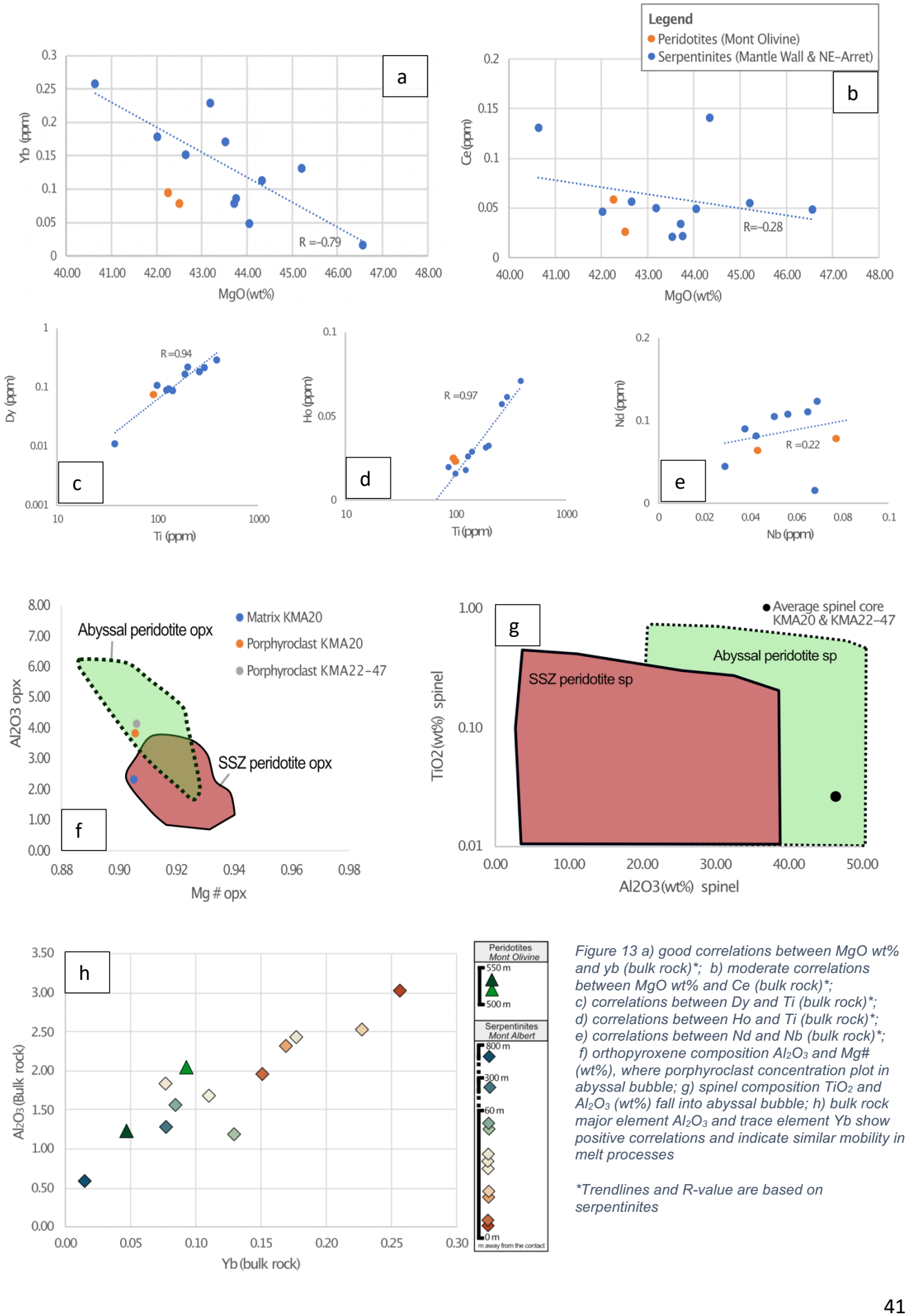

Figure 13 a) good correlations between MgO wt% and yb (bulk rock); b) moderate correlations between MgO wt% and Ce (bulk rock)*; c) correlations between Dy and Ti (bulk rock)*; d) correlations between Ho and Ti (bulk rock)*; e) correlations between Nd and Nb (bulk rock)*; f) orthopyroxene composition Al_2O_3 and Mg# (wt%), where porphyroclast concentration plot in abyssal bubble; g) spinel composition TiO_2 and Al_2O_3 (wt%) fall into abyssal bubble; h) bulk rock major element Al_2O_3 and trace element Yb show positive correlations and indicate similar mobility in melt processes*

**Trendlines and R-value are based on serpentinites*

4.2.3 Mantle rock mineral composition (In-situ)

Table 3 provides representative electron microprobe analyses for olivine, orthopyroxene, clinopyroxene, and spinel. Sample KMA20 from Mont Olivine contains no-limited fluid alterations and sample KMA22-47 from the NE Arrêt is partly serpentinized, but relict olivine, pyroxene, and cores of altered Cr-spinel allowed quantification of mineral chemistry.

Olivine

Chemical analysis for olivine indicate all samples are forsteritic (2 samples n= 48 single point measurements), with homogeneous compositions within single minerals, between minerals in thin sections, and between thin sections. KMA20 comprise a matrix of fine grained olivine and elongated olivine porphyroblasts with optically visible sub grains, for which the Mg# is identical with Fo=91.00 ± 0.00 (n=28). The textural and chemical composition of Mont Olivine is similar to the less serpentinized samples from the NE-Arête, with Fo=91.00 ± 0.00 (n=20). Minerals contain 0.41±0.01 wt% NiO (n=20) for KMA20 and 0.38±0.01 wt% NiO (n=28) for KMA22-47.

Orthopyroxene

Mineral analysis for orthopyroxene shows variable chemical composition for texturally different orthopyroxene (2 samples, n= 33 single point measurements). In sample KMA20, orthopyroxene is present as component of the fine grained matrix and as porphyroclasts, containing spinel inclusions and clinopyroxene exsolution lamellae. Both samples contain concentrations of 55.51 ± 0.6 (n=5) wt% SiO_2 for the matrix and 54.04±0.61 (n=28) wt% SiO_2 for the porphyroclasts. Concentrations are 0.8±0.1 (n=33) wt% NiO and 0.3±0.00 (n=33) wt%TiO_2, which are comparable for both samples and textures. Both textures have consistent Mg# = 0.91 ± 0.01 (n=17).

Grains that are part of the matrix have a relatively low Cr#=0.06±0.02 (n=5), compared to the porphyroclasts which have Cr#=0.10±0.07 (n=12). Due to heavy serpentinization of the matrix the chemical composition of orthopyroxene in KMA22-47 is only measurable in partly serpentinized porphyroclasts, for which the chemical composition is comparable with KMA20 in terms of Mg#=0.91±0.00 (n=16) and Cr#=0.10±0.00 (n=16). Concentrations of Al_2O_3 differ strongly between porphyroclasts and matrix textures for KMA20 with a lower 1.74±0.6 wt% Al_2O_3 for matrix and higher 3.71±0.39 wt% Al_2O_3 for porphyroclasts, which are similar to the NE-Arête porphyroclasts (Figure 13f). Matrix grains also contain a relatively low concentration of 0.27 ±0.17 (n=5) wt% Cr_2O_3 and porphyroclasts have a higher concentrations of 0.67 ±0.12 wt% Cr_2O_3.

Clinopyroxene

Mineral analysis for clinopyroxene shows relatively depleted chemical composition (2 samples, n= 33 single point measurements). Clinopyroxene is present as part of the fine grained matrix, as porphyroblasts and for KMA20 as exsolution lamellae in the orthopyroxene clasts. Analysis yields concentrations of 0.14±0.05 (n=33) wt% Na_2O, 0.08±0.01 (n=33) wt% TiO2, and 0.05±0.01 wt% NiO for both textures. Both samples yield high Mg#=0.94±0.01 (n=31) for single grains and exsolution lamellae. In both samples the Cr# is generally lower for single grains where Cr#=0.11±0.02 (n=15) and higher for the lamellae in KMA20 where Cr#=0.15±0.02 (n=6).

Spinel

Chemical analysis on Cr-spinel indicate variable composition for core and rim measurements (2 samples, n=81 single point measurements of which n_{core}= 36 and n_{rim}=45). Cr-spinel is present as micrometre-scale grains in the olivine/pyroxene matrix and as micrometre to nanometre-scale inclusions in the pyroxenes. For both samples, spinels contain 0.23±0.01 wt% NiO and very low 0.03±0.01 wt% TiO_2. Core composition of spinels in both samples is homogeneous with Cr#= 0.23±0.02 and Mg# = 0.67±0.01 (n=36).

Compared to the core chemistry, the chemical composition of the spinel far edges is more variable and exhibits lower Cr# and higher Mg# (Figure 14a and Figure 15a). These variations are concentrated in the elongated sides of the grain. Compared to core compositions, Mont Olivine rim measurements yield higher Mg#=0.72±0.04 (n=29), and lower Cr#=0.14±0.05 (n=29) of which four measurements exhibit extreme low values of Cr#=0.06±0.02 (n=4). Rim measurements of the NE-Arête sample yield less variability between measurements with Cr#=0.18±0.03 and Mg#=0.69±0.03 (n=16), but values are lower compared to core composition.

In conclusion, the Mont olivine peridotite has a more consistent core composition compared to the NE-Arête serpentinites, but shows more variability in rim composition throughout the section (Figure 15b/c).

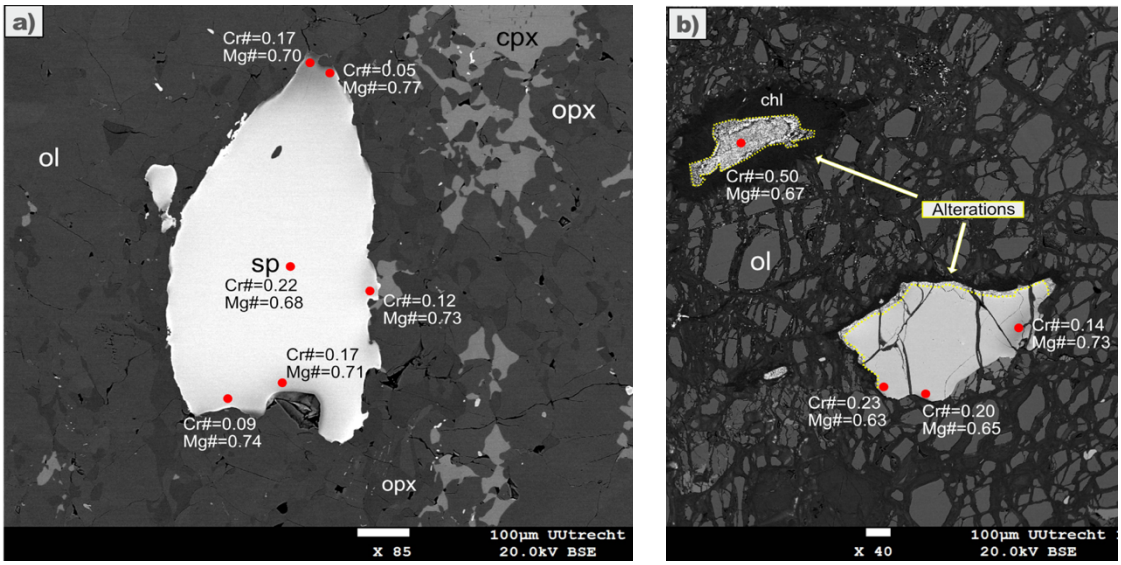

Figure 14 Core/rim composition of Cr-spinel in a) KMA20 (peridotite) and b) KMA22-47 (serpentinite). Yellow dotted line in b) indicates areas of Cr-spinel alterations into a chrome-chlorite.

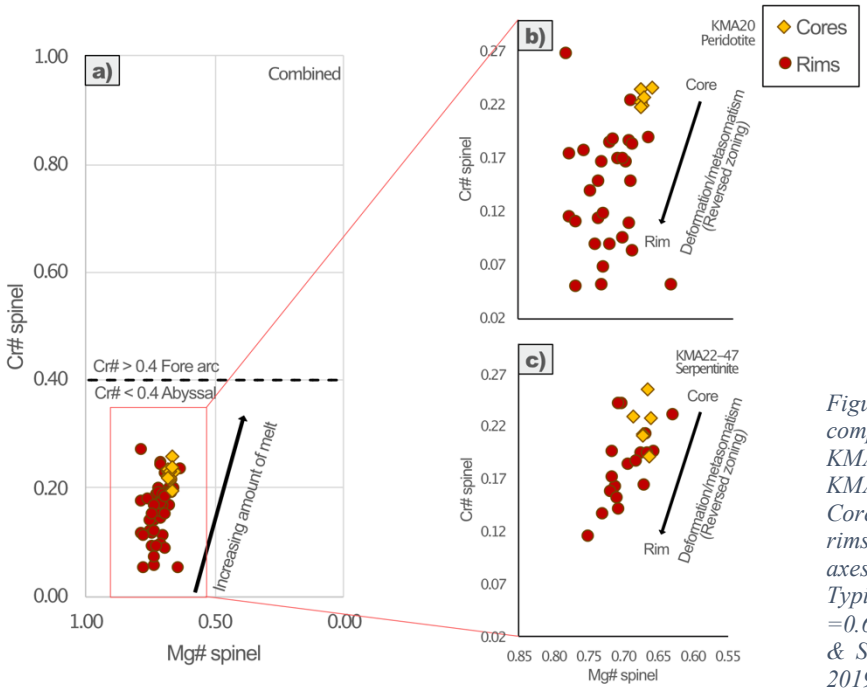

Figure 15 a) Combined core/rim composition of spinel minerals in b) KMA20 (top right, peridotite) and c) KMA22-47 (bottom right, serpentinite). Cores are plotted in red diamonds and rims in yellow circles. Note that the x-axes are plotted from high to low. Typically fore arc samples plot above Cr# =0.6 and abyssal below Cr# =0 (Ahmed & Surour, 2016; Gamal El Dien et al., 2019).

Table 3 Mineral compositions of olivine, spinel, orthopyroxene and clinopyroxene.

	Sample nr.	KMA20		KMA20		KMA22-47	
	Mineral	OPX		OPX		OPX	
	Texture	Matrix		Porphyroclast		Porphyroclast	
		Average	*stdev*	Average	*stdev*	Average	*stdev*
WT% calculat	SiO2	55.51	0.60	54.47	0.48	53.61	0.75
	TiO2	0.02	0.00	0.02	0.01	0.03	0.01
	Al2O3	2.32	1.02	3.82	0.69	4.15	0.26
	Cr2O3	0.27	0.17	0.66	0.12	0.67	0.06
	FeO	6.58	0.24	6.41	0.11	6.31	0.13
	MnO	0.15	0.02	0.14	0.01	0.14	0.01
	MgO	35.21	0.46	34.46	0.42	34.18	0.29
	CaO	0.32	0.13	0.37	0.14	0.53	0.31
	NiO	0.07	0.01	0.09	0.01	0.08	0.01
	Na2O	-0.01	0.01	-0.01	0.01	-0.01	0.00
	K2O	0.01	0.00	0.01	0.00	0.01	0.00
	TOTAL	100.45	0.26	100.43	0.23	99.70	0.86
atoms wt% fo	Si AT%	19.08	0.22	18.74	0.14	18.59	0.11
	Ti AT%	0.01	0.00	0.01	0.00	0.01	0.00
	Al AT%	0.94	0.41	1.55	0.28	1.69	0.11
	Cr AT%	0.07	0.05	0.18	0.03	0.18	0.02
	Fe AT%	1.89	0.07	1.84	0.03	1.83	0.03
	Mn AT%	0.04	0.01	0.04	0.00	0.04	0.00
	Mg AT%	18.04	0.24	17.67	0.20	17.67	0.09
	Ca AT%	0.12	0.05	0.14	0.05	0.20	0.12
	Ni AT%	0.02	0.00	0.02	0.00	0.02	0.00
	Na AT%	0.00	0.01	-0.01	0.00	-0.01	0.00
	K AT%	0.00	0.00	0.00	0.00	0.00	0.00
	O AT%	59.79	0.02	59.81	0.02	59.77	0.04
	TOTAL	100.00	0.00	100.00	0.00	100.00	0.00
	Cr#	0.07	0.02	0.10	0.02	0.10	0.00
	Mg#	0.91	0.00	0.91	0.00	0.91	0.00

	KMA20		KMA20		KMA22-47	
	CPX		CPX		CPX	
	Matrix		Exsolution		matrix	
	Average	*stdev*	Average	*stdev*	Average	*stdev*
SiO2	53.02	0.67	52.33	0.81	52.85	0.80
TiO2	0.07	0.01	0.08	0.01	0.07	0.02
Al2O3	2.27	0.91	3.21	1.18	2.53	1.08
Cr2O3	0.44	0.21	0.84	0.23	0.55	0.29
FeO	1.97	0.17	2.27	0.89	2.06	0.48
MnO	0.07	0.01	0.07	0.01	0.07	0.01
MgO	17.79	0.50	18.52	2.90	18.02	1.55
CaO	24.36	0.39	22.23	4.86	23.74	2.64
NiO	0.04	0.01	0.05	0.01	0.05	0.01
Na2O	0.14	0.05	0.14	0.04	0.14	0.05
K2O	0.01	0.00	0.01	0.00	0.01	0.00
TOTAL	100.17	0.30	99.75	0.98	100.08	0.59
Si AT%	19.22	0.20	18.99	0.28	19.18	0.22
Ti AT%	0.02	0.00	0.02	0.00	0.02	0.00
Al AT%	0.97	0.39	1.38	0.51	0.98	0.35
Cr AT%	0.13	0.06	0.24	0.07	0.13	0.07
Fe AT%	0.60	0.05	0.69	0.27	0.61	0.05
Mn AT%	0.02	0.00	0.02	0.00	0.02	0.00
Mg AT%	9.61	0.24	10.02	1.56	9.63	0.18
Ca AT%	9.46	0.16	8.64	1.89	9.49	0.14
Ni AT%	0.01	0.00	0.02	0.00	0.01	0.00
Na AT%	0.10	0.04	0.10	0.03	0.07	0.04
K AT%	0.00	0.00	0.00	0.00	0.00	0.00
O AT%	59.87	0.01	59.88	0.02	59.86	0.02
TOTAL	100.00	0.00	100.00	0.00	100.00	0.00
Cr#	0.11	0.02	0.15	0.02	0.11	0.03
Mg#	0.94	0.01	0.94	0.01	0.94	0.00

	Sample nr.	KMA20		KMA20		KMA22-47		KMA22-47	
	Mineral	Spinel		Spinel		Spinel		Spinel	
	Core/rim	Cores		Rims		Cores		Rims	
		Average	*stdev*	Average	*stdev*	Average	*stdev*	Average	*stdev*
WT% calculat	SiO2	-0.01	0.00	0.01	0.01	-0.01	0.01	0.00	0.01
	TiO2	0.03	0.00	0.02	0.01	0.03	0.01	0.03	0.01
	Al2O3	47.03	0.66	55.12	5.11	46.80	1.99	50.13	3.20
	Cr2O3	20.56	0.54	13.12	4.80	19.97	1.62	17.08	3.12
	Fe2O3	1.71	0.23	0.85	0.53	2.34	0.41	1.71	0.81
	FeO	14.14	0.22	12.62	1.48	14.33	0.26	13.46	1.18
	MnO	0.13	0.01	0.11	0.02	0.14	0.01	0.12	0.02
	MgO	16.49	0.21	18.43	1.37	16.29	0.38	17.18	0.93
	CaO	0.00	0.00	0.00	0.03	0.00	0.01	0.00	0.01
	NiO	0.23	0.01	0.31	0.07	0.24	0.01	0.26	0.04
	Na2O	0.00	0.00	0.00	0.01	0.00	0.01	0.00	0.01
	K2O	0.01	0.00	0.01	0.00	0.01	0.00	0.01	0.00
	TOTAL	100.32	0.31	100.52	0.40	100.05	0.24	99.98	0.29
atoms wt% fo	Si	0.00	0.00	0.00	0.00	0.00	0.00	0.00	0.00
	Ti	0.00	0.00	0.00	0.00	0.00	0.00	0.00	0.00
	Al	1.52	0.02	1.71	0.11	1.52	0.05	1.60	0.08
	Cr	0.45	0.01	0.28	0.11	0.43	0.04	0.37	0.07
	Fe3+	0.03	0.00	0.02	0.01	0.05	0.01	0.03	0.02
	Fe2+	0.32	0.01	0.28	0.04	0.33	0.01	0.30	0.03
	Mn	0.00	0.00	0.00	0.00	0.00	0.00	0.00	0.00
	Mg	0.67	0.01	0.72	0.04	0.67	0.01	0.69	0.03
	tot. Cat.	3.00	0.00	3.00	0.00	3.00	0.00	3.00	0.00
	tot. Oxy.	4.00	0.00	4.00	0.00	4.00	0.00	4.00	0.00
	Cr#	0.23	0.01	0.14	0.05	0.22	0.02	0.19	0.04
	Mg#	0.68	0.01	0.72	0.04	0.67	0.01	0.69	0.03

	KMA20		KMA22-47	
	Ol		Ol	
	Matrix		Matrix	
	Average	*stdev*	Average	*stdev*
SiO2	39.78	0.22	39.88	0.19
TiO2	0.00	0.01	0.00	0.01
Al2O3	-0.01	0.01	0.00	0.01
Cr2O3	0.00	0.01	0.00	0.01
FeO	9.23	0.12	9.07	0.15
MnO	0.13	0.01	0.13	0.01
MgO	50.71	0.22	50.80	0.21
CaO	0.00	0.00	0.00	0.00
NiO	0.41	0.01	0.38	0.01
Na2O	-0.01	0.01	-0.01	0.01
K2O	0.01	0.00	0.01	0.00
TOTAL	100.24	0.37	100.26	0.33
Si AT%	13.87	0.04	13.89	0.04
Ti AT%	0.00	0.00	0.00	0.00
Al AT%	0.00	0.00	0.00	0.00
Cr AT%	0.00	0.00	0.00	0.00
Fe AT%	2.69	0.04	2.64	0.04
Mn AT%	0.04	0.00	0.04	0.00
Mg AT%	26.36	0.04	26.38	0.05
Ca AT%	0.00	0.00	0.00	0.00
Ni AT%	0.11	0.00	0.11	0.00
Na AT%	-0.01	0.00	-0.01	0.01
K AT%	0.00	0.00	0.00	0.00
O AT%	56.93	0.02	56.94	0.02
TOTAL	100.00	0.00	100.00	0.00
Fo	0.91	0.02	0.91	0.00

5. Discussion

5.1 Chemical constraints on tectonic setting of peridotite and sole formation

Selected fluid-immobile major, trace, and REE signatures of Mont Albert peridotites and serpentinites are most consistent with an oceanic abyssal mantle origin. These signatures do not reflect formation of a well-developed SSZ mantle wedge, but rather show the preservation of abyssal lithosphere as a component of an underdeveloped mantle wedge. Average spinel core composition of Cr#=0.23 ± 0.01 (n=30) is low and indicative of limited melting that is typically found in an abyssal setting, in contrast to a high degree of melting that is typically found in mantle wedge peridotites (Figure 16). Spinel core composition plots in the Olivine-Spinel-Mantle-Array (OSMA), as defined by Arai (1994), which implies the chemistry of these minerals reflects the original protolith mantle and can be used as a tectonic setting diagnostic (Dick & Bullen, 1984). Additionally, Mont Albert spinels show a fresh composition with limited core/rim variation and thus is reliable to use as a tectonic indicator. Additionally, concentrations of Al_2O_3 in spinel and orthopyroxene porphyroclasts are most consistent with abyssal origin (Figure 13f & 13g).

Similar to how spinel preserves magmatic depletion signatures, the bulk rock REEs are relatively incompatible in all present phases (ol, opx, cpx) and thus also reflect original melt residue signatures in the mantle (Niu, 2004). In agreement with the spinel composition, spider diagrams of REE and high concentrations of Ti>50 ppm are most consistent with average abyssal datasets, and do not overlap with a well-developed depleted mantle wedge (Figure 17) (Deschamps et al., 2013). Spider diagrams also overlap with “subducted serpentinites”, but can be ruled out by our structural observations that demonstrate Mont Albert preserves an in-tact subducting crust-upper plate mantle contact. Furthermore, the combination of peak metamorphic conditions that exceed serpentine stability and the absence of the high-T polymorph antigorite, are together indicative of late stage serpentinization.

Relatively depleted REE concentrations further support an oceanic lithosphere setting, as opposed to a subcontinental lithosphere. Analysis of continental lithosphere xenoliths generally show more fertile trace element compositions and a sharp increase in LREE concentrations compared to MREE and HREE, which is not the case for Mont Albert (Downes, 2001). The presence of a positive slope from LREE to HREE and low concentrations of Th/Yb = ± 0.1 are more consistent with an oceanic formation setting (De Hoog et al., 2009; Deschamps et al., 2013; Franqui et al., 2017; Jochum et al., 1989; Niu, 2004; Pearce, 1982).

An abyssal formation setting is further suggested by anhydrous major element ratios MgO/SiO_2 and Al_2O_3/SiO_2 which are often used to infer a melting trend, since MgO retains

magmatic signature and both ratios are not affected by serpentinization (Niu, 2004; Paulick et al., 2006; Snow & Dick, 1995). Samples plot on the terrestrial melting array, characterizing a progressive melt extraction from depleted mantle and show very limited impact from talc/brucite formation, seafloor weathering or carbonation (Kodolányi et al., 2012; Snow & Dick, 1995). A wide spread in Al_2O_3/SiO_2 is more often seen for abyssal serpentinites, as mantle wedge compositions more typically plot towards a lower Al_2O_3/SiO_2 and a higher MgO/SiO_2. As shown by Deschamps (2013) these ratios cannot be conclusively used as a diagnostic for tectonic setting, but they are in line with spinel mineral composition and bulk rock HREE.

The presence of abyssal peridotite occupying a fore-arc mantle position is not uncommon; chemical signatures that are consistent both with abyssal formation and subsequent evolution in a fore-arc are seen in the Bay of Islands, Semail, and Thetford mines ophiolites (Figure 16) (Pagé et al., 2008; Stern, 2013; Takazawa et al., 2003). All locations present a range in Cr# and trace elements, indicating variable melt depletion. For all these ophiolite bodies, this variation is interpreted to represent the evolution of abyssal to mantle wedge peridotite in a developing/aging subduction zone (Stern, 2013; Yoshikawa et al., 2015). The large variation in Cr# (0.2-0.7) seen in the other ophiolite localities was not observed in my sample suite for Mantle Wall and Mont Olivine, but previous research on Mont Albert peridotites by MacGregor & Basu (1979) has indicated that higher and more variable Cr# are found further south (structurally higher) into the peridotite body. Therefore it might be possible that a fore-arc signature is preserved further into the Mont Albert mantle sequence. Another explanation is that Mont Albert represents an extremely heterogeneous abyssal peridotite; while high Cr# (Cr# >0.4) are more often seen in fore-arc peridotites, these values can also occur in abyssal peridotites (J. Warren, 2016).

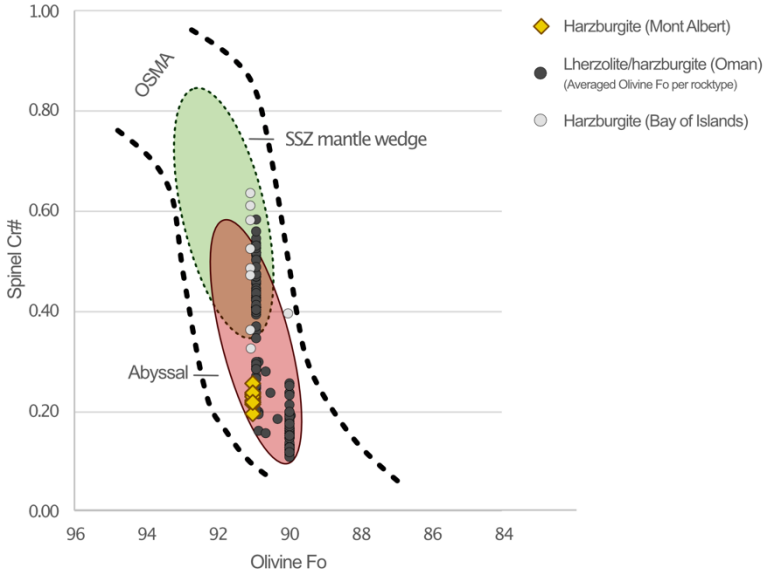

Figure 16 Spinel Cr# versus. Olivine Mg#. Mantle Wall samples are indicated by red diamonds and are compared to lherzolites/harzburgites from Oman taken from (Khedr et al., 2014; Takazawa et al., 2003) and harzburgites from Bay of Island, Newfoundland from (Stern, 2013). Fields for SSZ mantle wedge and abyssal indicate where the average global datasets fall. Figure modified from Arai (1994) and Khedr et al. (2014).

Similar geochemical analysis can be done for the sole rock to infer the type of basaltic protolith for the subducting crust. Trace element values yield low ratios of 11 < Ti/V < 22, but high values for V=~400 ppm indicate formation in a mid-oceanic ridge setting or a back arc basin (Pearce & Norry, 1979; Shervais, 1982). This is fitting with the tectonic setting for the mantle rock and is in accordance with the interpretation that the sole is the metamorphic equivalent of the sub-alkaline an tholeiitic Shick-Shock volcanics (Dubacq et al., 2019).

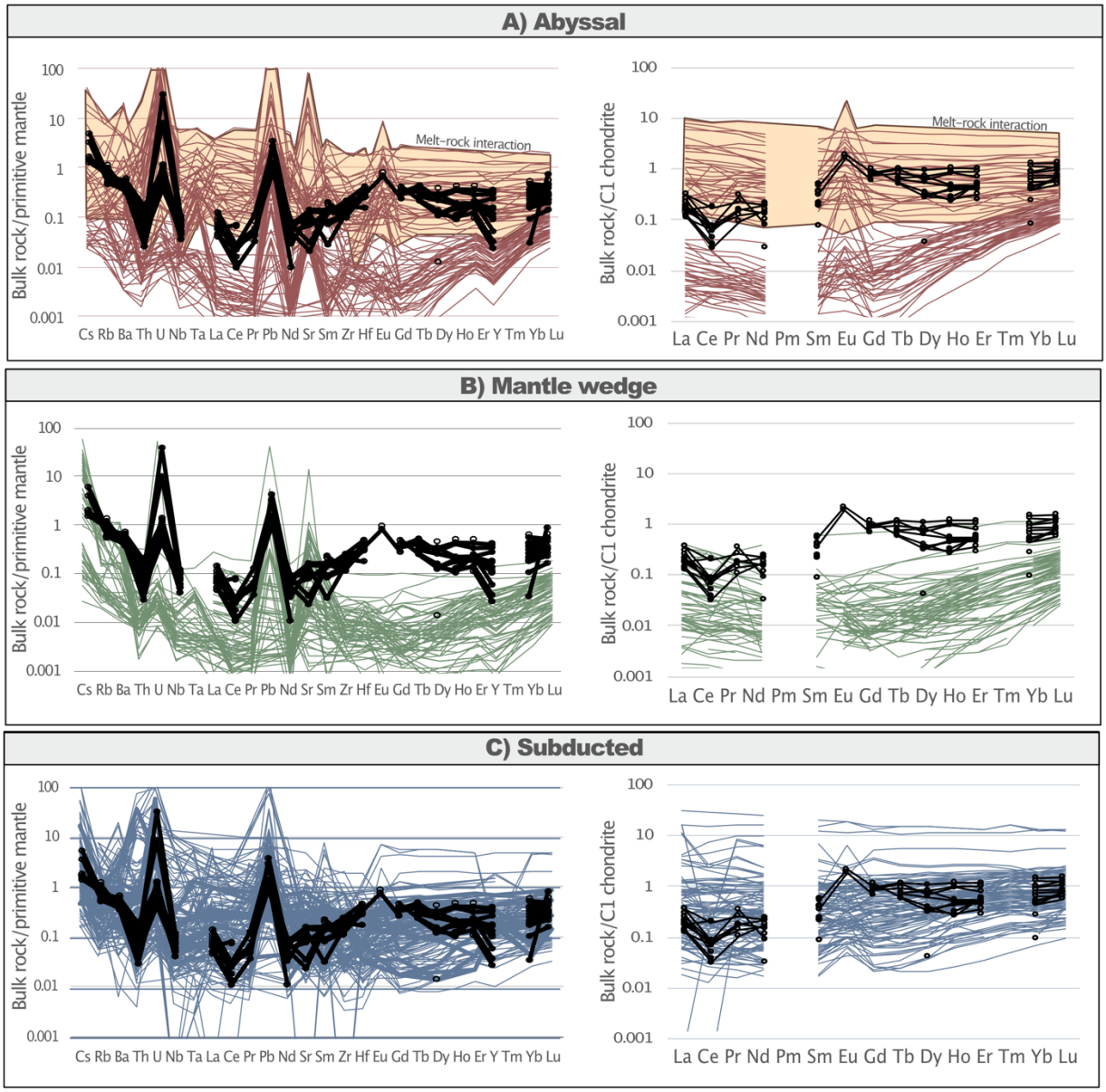

Figure 17 Multi-element and REE patterns compared to compiled datasets by Deschamps 2013. Mont Albert concentrations are shown in black. The abyssal dataset can be separated into two subsets corresponding to depleted mantle and refertilized abyssal composition due to melt-rock interactions (indicated in orange field).

5.2 Trends in melt depletion with structural distance from the sole-mantle contact

Anhydrous ratio Al_2O_3/SiO_2 and incompatible HREEs (Do, Er, Yb, Lu) indicate an increase in melt depletion with increasing structural height away from the slab-mantle contact. This apparent relationship is best explained by the presence of a pre-existing compositional heterogeneity, in the form of magmatic layering, in the abyssal protolith. Major element MgO is an excellent magmatic indicator. Geochemical data presented above reveals positive correlations between MgO, HFSE, and HREE, indicating that all can be used as tracers of magmatic depletion (Fig 13a,b,c,d) (Hellebrand et al., 2001; Niu, 2004). In addition, positive correlations between Yb (bulk rock) and Al_2O_3 (bulk rock) imply similarity in their partitioning behaviour during magmatic processes (Figure 13h).

Melt depletion trends show a strong gradient within a structural thickness of 60 m of the contact, where samples structurally higher generally have the highest degree of melt depletion (15%) and samples close to the contact the lowest (5%). The question, therefore, is what caused such extreme changes in melt depletion over such a small structural interval – melting before, or melting during/after subduction initiation? Although slab dehydration induces partial melting in the mantle wedge in mature subduction zones, for Mont Albert this cannot cause the magmatic layering, considering the P-T conditions across the contact. Peak P-T conditions in the metamorphic sole during accretion to the peridotites are estimated at 1-1.2 GPa (~30-40 km) and 850 °C (Dubacq et al., 2019). Conditions of the mantle deformation are more difficult to constrain, but dynamic recrystallization of the peridotites occurred in the spinel stability field and therefore at maximum P of 1.5 GPa (Perkins & Anthony, 2011). Dynamic recrystallization of the matrix may explain the observed compositional differences between lower-Al pyroxene matrix grains and higher-Al porphyroclasts, as well as the minor zoning in the spinel, with increased Al_2O_3 contents forming at spinel rims along the lineation direction (Figure 13 & 15). In line with the peak temperatures for the sole, temperatures for sub-solidus mantle recrystallization have been previously estimated for Mont Albert peridotites by Bazylev & Silantyev (2000) at T = 754-894 °C. Therefore, similar peak P-T estimates across the sole-mantle contact point to minimal tectonic movement along the plate boundary since initial underthrusting. Furthermore, estimated temperatures are much too low for hydrous or anhydrous melting (Gaetani & Grove, 1998; Ulmer, 2001). Thus it is unlikely that large scale partial melting affected the Mont Albert peridotites after subduction initiation. This confirms that all observed mantle heterogeneity formed before subduction. The very thin structural interval of high-degree magmatic heterogeneity may indicate that tectonic thinning of the basal mantle occurred during high-T mantle shearing at the base of

the ophiolite, thus condensing an originally km's-thick interval into a zone <100 m thick (cf. Haessig et al., 2016).

5.3 No further melt extraction or infiltration following subduction initiation

The observed percentages of 5-15% melt extraction can either indicate original low degrees of melting, or a high degree of melting with subsequent refertilization (J. Warren, 2016). No conclusive melt refertilization is observed in the Mont Olivine peridotites, thus the first scenario is more likely. However, the low percentages of melt extraction and lack of melt-rock interaction after subduction is surprising compared to neighbouring Thetford Mine ophiolite (Pagé et al., 2008). Compared to Mont Albert, the Thetford Mine ophiolite is a sliver of further developed mantle wedge, as indicated by the abundant textural evidence for melt-rock interaction and its proximity to the Ascot volcanic (proto-)arc complex. Comparisons between these two temporally- and genetically-related Appalachian ophiolites further demonstrates that different portions of the mantle experienced different melt histories depending on their proximity to ophiolite fore-arc spreading centers.

Melt refertilization would impart characteristic chemical and textural signatures to the peridotites, which was not observed in the Mont Albert samples. Since LREE are more easily mobilized than HREE, enrichment in these elements are often used to infer about melt refertilization (Gaetani & Grove, 1998; Niu, 2004). Unfortunately analysis of bulk rock LREE concentrations is often difficult, since elements are easily mobilized by fluids. For Mont Albert, concentrations of La and Ce (LREE) likely portray original magmatic formation, but Nd and Pr (LREE) show inconclusive correlations. In-situ pyroxene trace element analysis would be a more conclusive method to asses element mobility (Hellebrand et al., 2001; J. M. Warren & Shimizu, 2010). However, mineral compositions of spinel and orthopyroxene have extremely low concentrations of TiO_2 and Na_2O in spinel and pyroxenes which indicate a depleted nature, rather than an enriched one.

Petrographic observations also support no or limited melt infiltration. No interstitial spinel or clinopyroxene has been observed for Mont Olivine peridotite, as is seen in Thetford mines (Pagé et al., 2008). In two samples, orthopyroxene porphyroclasts are replaced by coarse grained olivine and orthopyroxene (Figure 6b). The same texture was observed in the Semail ophiolite and interpreted as evidence for partial melting under low pressures or melt infiltration reactions (Yoshikawa et al., 2015). The reaction is only observable for two Mont Albert serpentinites. The recrystallized matrix in the unserpentinized Mont Olivine peridotite shows bulging grain boundaries and phase mixing, which are sometimes interpreted as melt textures (Dijkstra et al.,

2002), but could also be linked to fluid assisted strain localization (Hidas et al., 2016). Combining these chemical and textural observations with the temperature constraints it is most likely that dynamic recrystallization of (wet?) olivine is responsible for the observed texture. Overall, the chemistry of Mont Albert is most similar to the more depleted Type 1 lherzolites from the Semail ophiolite that underwent melt depletion and metasomatism but without significant melt-rock interaction (Takazawa et al., 2003; Yoshikawa et al., 2015).

5.4 Limited fluid mobile element overprinting during serpentinization

Despite penetrative serpentinization in the first ~20 structural meters above the contact at Mantle Wall, original mantle chemical signatures are preserved in the samples, which has implications for the mobility of FMEs in this system. The presence of iron-oxide rich lizardite serpentinites in the contact zone mylonites indicates a late-stage, low-temperature (<300˚C; Guillot and Hattori, 2013), oxidizing serpentinization process. The Mantle Wall sequence is characterized by a decrease in degree of serpentinization with structural height from the contact which is observable with optical microscopy, despite high L.O.I. contents throughout the section. The presence of ribbon textured serpentine indicates serpentinization was not a simple static overprint, but was part of a deformation event.

Similar to how fluid-immobile HREE are used to infer magmatic processes, the fluid-mobile elements are typically used for interpreting fluid metasomatism (Deschamps et al., 2013; Peters et al., 2017; Scambelluri et al., 2004). In the Mont Albert samples, concentrations of Pb, As, Cs and Ba are high, which is often an indication for crust derived fluids, where fluid is transferred from slab to mantle wedge (Hattori et al., 2005; Scambelluri et al., 2019). However, the same samples show high concentrations of U, which is not typically seen in fore-arc serpentinites, but almost always in oceanic mantle serpentinization (Peters et al., 2017). Plotting the Mont Albert FME concentrations in discriminatory figures by Peters (2017) does not conclusively indicate the tectonic setting of serpentinization (Figure 5); concentrations and ratios of Cs, U, and Rb plot in between average abyssal and fore-arc settings. This implies that with this chemical dataset, the tectonic environment of serpentinization and origin of fluids cannot be determined. However, structural observations demonstrate without question that serpentinization must have occurred along an existing plate interface, in a (proto-)forearc position.

What is surprising is that in both peridotites and serpentinites from Mont Albert, concentrations of FME (U, Pb, As, Cs, Ba, Rb) show the same enrichments with extremely similar concentrations, indicating that despite near-complete serpentinization, the original peridotite chemistry is preserved (peridotite concentrations are highlighted in Figure 18). While enrichment

trends are similar for both fresh and altered rock units, it can be argued that the overall FME concentrations are 0-20% higher for most serpentinites, especially for Pb, Ba and Sr (Figure 18). Even so, the overprint is limited. Either the fluid causing serpentinization was in geochemical equilibrium with the host rock and caused no elemental exchange, or there simply was a very limited FME cycling between fluids and the host rock during serpentinization. “Isochemical” serpentinization is commonly seen in formation of lizardite, where mineral structure prevents the incorporation of trace elements (type 1 lizardite of Ulrich et al., 2020). This could be an explanation for the very limited chemical difference between peridotite and serpentinites.

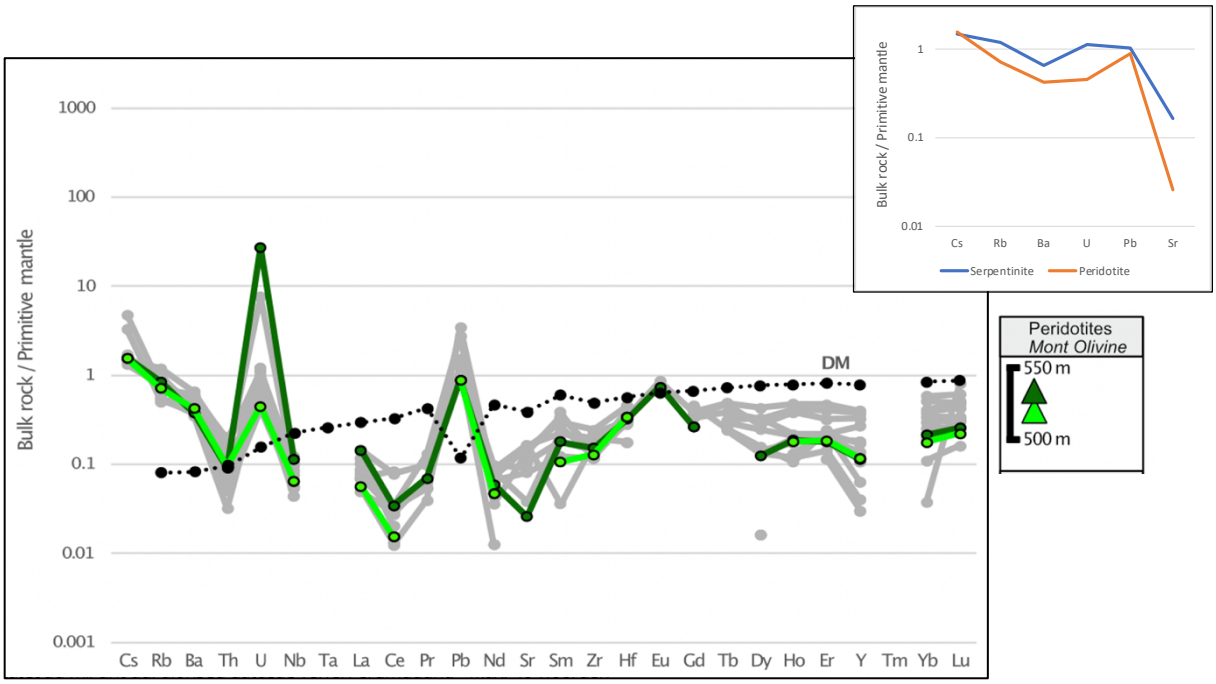

Figure 18 Zoom in on difference in FME concentrations between sample with the highest level of serpentinization (KMA22-03) and fresh peridotite (KMA20). Topright: A selection of FME (Cs, Rb, Ba, U, Pb, Sr – ordered on increasing compatibility) show the very limited difference in element concentrations between the structurally lowest serpentinite (near 100 % serpentine by volume) and peridotite.

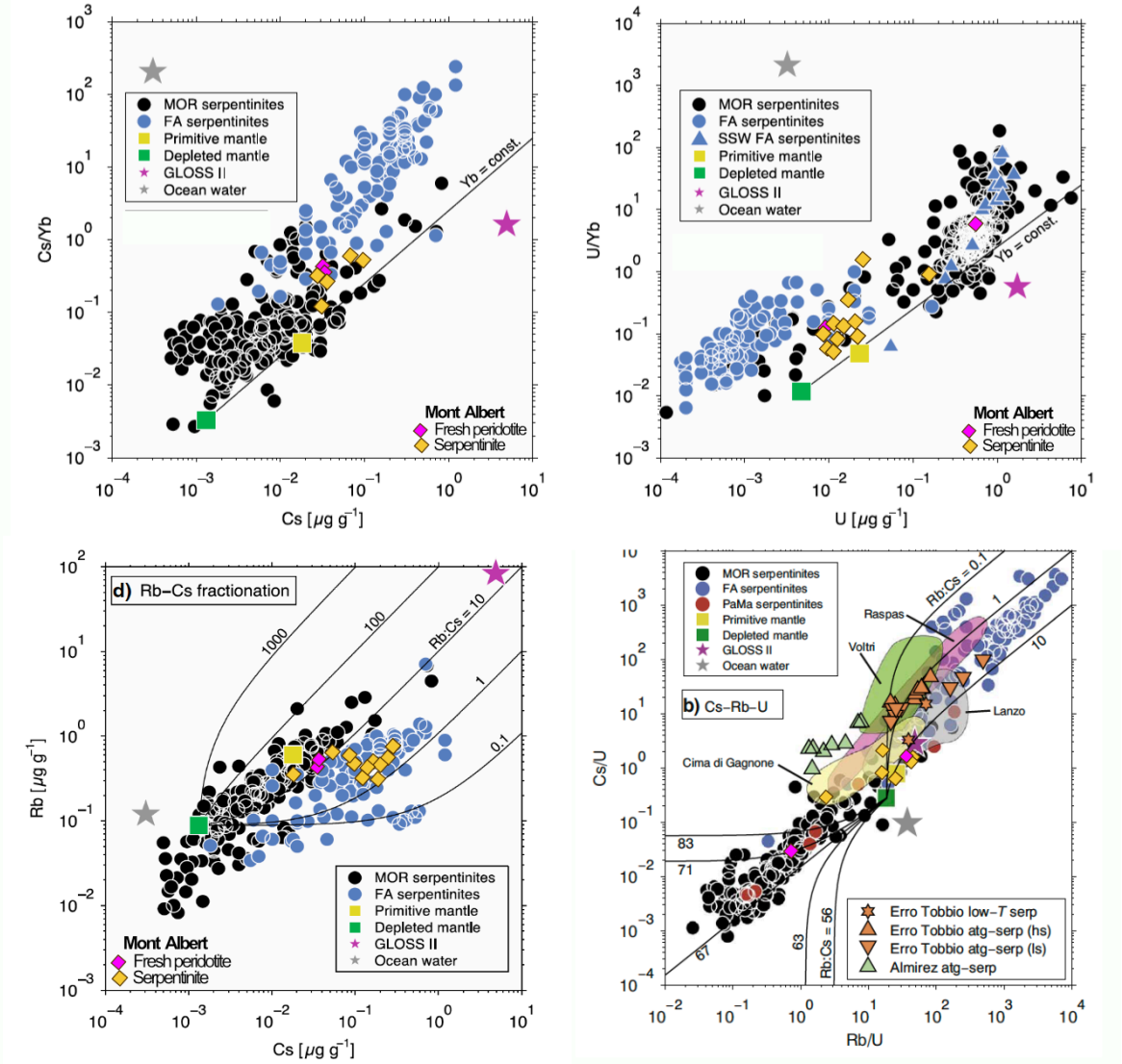

Figure 19 Trace element concentrations and ratios plotted in discriminatory plots from Peters (2017). Datapoints are compared to mid oceanic ridge (MOR – in black) and fore arc (FA – in blue) setting.

5.5 Implications for strain localization during subduction initiation

The plate contact preserved around the northern rim of Mont Albert formed during the first developmental stages of a new Ordovician subduction zone and underwent limited melt and trace element cycling during its infant stages. Figure 20 illustrates the conceptual model of Mont Albert's evolution from 1) a pre-existing, chemically heterogeneous oceanic lithospheric mantle to 2) the first stages of subduction and coupling of subducting slab to the mantle. Intra-oceanic subduction initiation and sinking of the Iapetus Ocean was induced by far-field tectonic forces that eventually resulted in convergence with Laurentia. Serpentine minerals are often discussed as strain-localizing agents during subduction initiation and shear zone formation (Hirth & Guillot, 2013; Maffione et al., 2015; Wintsch et al., 1995), but structural and geochemical data demonstrate that serpentinization of Mont Albert peridotites occurred well after the plate boundary was established. Therefore, during initial underthrusting, plate boundary strain localization may have preferentially occurred along a zone of layered mantle magmatic heterogeneity. This hypothesis is supported by the observation that preserved chemical layering at Mantle Wall is concordant with the plate interface. The possible relation between mantle heterogeneity and subduction initiation has been

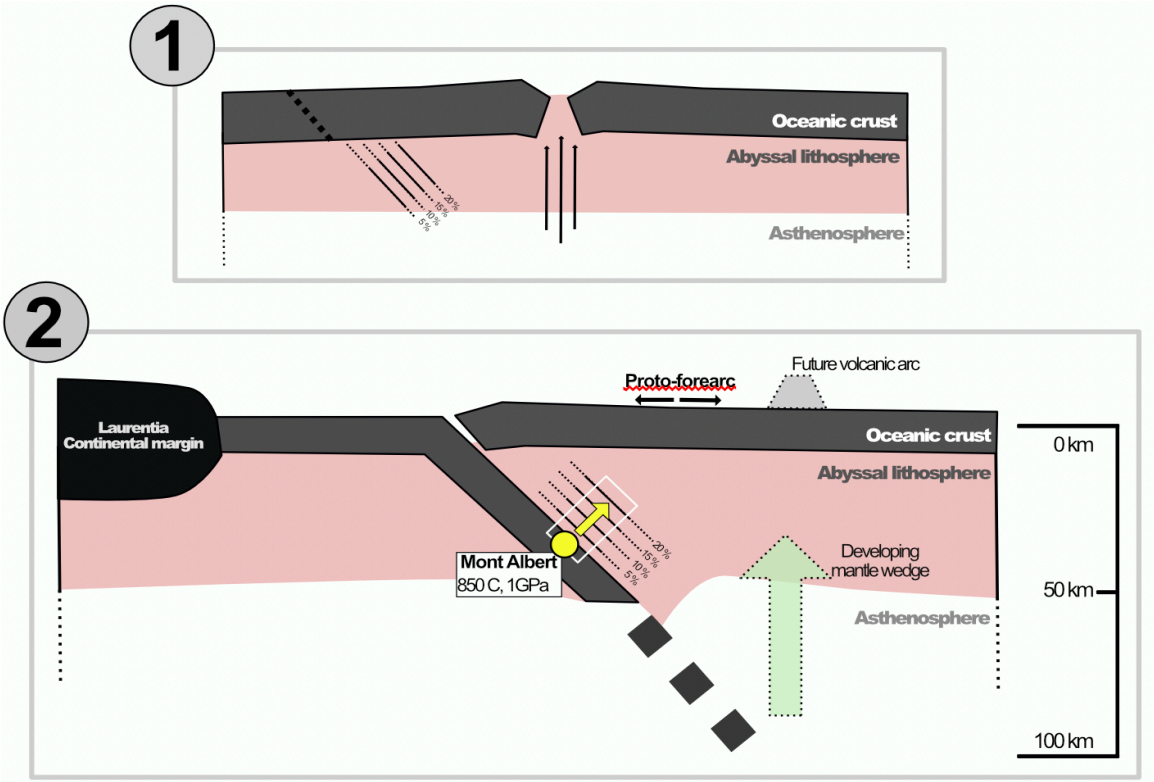

Figure 20 Conceptual image portraying the evolution of 1) heterogeneous abyssal lithosphere in MOR setting; 2) after subduction initiated. The estimated location of Mont Albert, with sole rock and Mantle Wall sequence is indicated in white box and yellow. Mont Albert is indicated with known temperature and depth constraints. Note that more heterogeneity in the oceanic lithosphere is likely, and only the heterogeneity that is confirmed in this research is indicated in this illustration.

discussed before (Anderson, 2006), but the effect of compositional heterogeneity on the mechanical behaviour of the lithospheric mantle is considered to be low (Chenin et al., 2019; Tommasi & Vauchez, 2015). Thus, whether the plate boundary chose to localize along pre-existing weaknesses in a heterogeneous mantle remains to be tested, but regardless, serpentinite did not play a leading role.

5.7 Future work

Previous research suggests even more chemical variability is present in the peridotite body of Mont Albert than what is already shown by the Mantle Wall, Mont Olivine, and NE Arête samples (Bazylev & Silantyev, 2000; MacGregor & Basu, 1979). A more complete representation of the chemical variation along the structural transect requires further analysis on samples collected from higher structural levels above the contact. Because Mont Albert provides such an ideal window into the tectonic evolution of the coupled sole rock and peridotite, the chemical variation along the contact can give more constraints on the conditions favoring rheological coupling between sole and mantle. In-situ REE concentrations of ortho- and clinopyroxene, as opposed to bulk rock, would further assess melt equilibrium without the “noise” of fluid metasomatism enrichments (J. M. Warren & Shimizu, 2010). Analyses on interstitial spinel and clinopyroxene mineral compositions, compared to porphyroclasts, would constrain possible melting and recrystallization processes of the matrix. Mont Albert trace elements concentrations do not give conclusive answers in determining the exact conditions of serpentinization, but Boron or Oxygen isotopes can help in determining the tectonic setting and origin of fluids in the serpentinization process (Martin et al., 2020). Similar analyses have been done for the Semail ophiolite, and reveal that fluids are delivered via channelized conduits and are crust-derived (Prigent, Guillot, Agard, Lemarchand, et al., 2018; Yamaoka et al., 2012). My study therefore provides crucial first-order structural, microstructural, and chemical context that future studies will undoubtedly build on.

6. Conclusion

Subduction infancy is a critical, but poorly understood, stage of a subduction zone development. This study has explored how microstructures and geochemistry change in the upper plate mantle lithosphere during the very first stages of subduction. Together, these features provide deeper insight into how the lithosphere evolves as a subduction plate boundary shear zone develops. The mantle section of the ophiolite body of Mont Albert (Québec, Northern Appalachians, Canada) is characterized by a transition of ultra-mylonitic serpentinite to porphyroclastic peridotite, that is interpreted to represent a supra-subduction zone mantle wedge. My results show that the mantle peridotite chemistry is characteristic of an abyssal peridotite and shows signs of a mid-oceanic ridge history before subduction initiation. I infer that Mont Albert represents a piece of original abyssal mantle that is preserved in what is now a fore-arc position, in present configuration. Mantle composition shows a strong gradient from 5 to 15 % melt depletion over a 60 m structural interval, traversing perpendicular to the foliation which is parallel to the slab-mantle contact (i.e., the paleo-plate interface). I interpret this gradient in depletion to be a relict of the heterogeneity of original abyssal lithosphere. I conclude that the heterogeneity is not formed by subduction-induced melting of the mantle wedge, nor was it altered during subsequent melt-rock reactions. After subduction initiation, a late stage, low temperature serpentinization resulted in a lizardite front parallel to the slab-mantle contact. Geochemical analyses on the lizardite serpentinites reveal that trace element incorporation during fluid alteration was very limited, because similar FME concentrations were measured in the fresh peridotites and the fully serpentinitized mantle rocks. These results demonstrate that the stage of subduction zone development and thermal structure together exert first-order control on mantle wedge composition and its evolution. Particularly, we infer that Mont Albert Mantle Wall represents the ‘cold corner’ which is structurally and chemically distinct from arc-proximal locations where more melting occurs. Comparison of mantle wedge chemistry should always be accompanied by structural context. Exhumed ophiolites play a key role in understanding subduction processes and, when geochemical studies are contextualized by structural observations, can provide crucial insight into mechanical, magmatic, and metasomatic evolution of mantle wedge lithosphere.

References

Abbey, S. (1983). Studies in 'Standard Samples' of silicate rocks and miinerals 1962-1982: Geological Survey of Canada Paper 83-15. *Geological Survey of Canada Paper 83-15*, 1–114.

Alcock, F. J. (1927). *La région cartographiée du Mont Albert, Québec*.

Anderson, D. L. (2006). Speculations on the nature and cause of mantle heterogeneity. *Tectonophysics*, *416*(1), 7–22. https://doi.org/10.1016/j.tecto.2005.07.011

Arai, S. (1994). Characterization of spinel peridotites by olivine-spinel compositional relationships: Review and interpretation. *Chemical Geology*, *113*(3), 191–204. https://doi.org/10.1016/0009-2541(94)90066-3

Bazylev, B., & Silantyev, S. (2000). Geodynamic interpretation of the subsolidus recrystallization of mantle spinel peridotites: 2. Ophiolites and xenoliths. *Petrology*, *8*, 311–331.

Beaudin, J. (1986). *Analyse structurale du Groupe des Shickshock et de la péridotite alpine du mont Albert, Gaspésie*. Bibliothèque nationale du Canada.

Camiré, G., La Flèche, M. R., & Jenner, G. A. (1995). Geochemistry of pre-Taconian mafic volcanism in the Humber Zone of the northern Appalachians, Québec, Canada. *Chemical Geology*, *119*(1), 55–77. https://doi.org/10.1016/0009-2541(94)00104-G

Cerpa, N. G., Wada, I., & Wilson, C. R. (2017). Fluid migration in the mantle wedge: Influence of mineral grain size and mantle compaction. *Journal of Geophysical Research: Solid Earth*, *122*(8), 6247–6268. https://doi.org/10.1002/2017JB014046

Chenin, P., Picazo, S., Jammes, S., Manatschal, G., Müntener, O., & Karner, G. (2019). Potential role of lithospheric mantle composition in the Wilson cycle: A North Atlantic perspective. *Geological Society, London, Special Publications*, *470*(1), 157–172. https://doi.org/10.1144/SP470.10

Church, W. R. (1977). The ophiolites of southern Quebec: Oceanic crust of Betts Cove type. *Canadian Journal of Earth Sciences*, *14*(7), 1668–1673. https://doi.org/10.1139/e77-141

Dallmeyer, R. D., & Hibbard, J. (1984). Geochronology of the Baie Verte Peninsula, Newfoundland: Implications for the Tectonic Evolution of the Humber and Dunnage Zones of the Appalachian Orogen. *The Journal of Geology*, *92*(5), 489–512.

De Hoog, J. C. M., Janák, M., Vrabec, M., & Froitzheim, N. (2009). Serpentinised peridotites from an ultrahigh-pressure terrane in the Pohorje Mts. (Eastern Alps, Slovenia): Geochemical constraints on petrogenesis and tectonic setting. *Lithos*, *109*(3), 209–222. https://doi.org/10.1016/j.lithos.2008.05.006

Deschamps, F., Godard, M., Guillot, S., & Hattori, K. (2013). Geochemistry of subduction zone serpentinites: A review. *Lithos*, *178*, 96–127. https://doi.org/10.1016/j.lithos.2013.05.019

Dewey, J. F., & Casey, J. F. (2013). The sole of an ophiolite: The Ordovician Bay of Islands Complex, Newfoundland. *Journal of the Geological Society*, *170*(5), 715–722. https://doi.org/10.1144/jgs2013-017

Dick, H. J. B., & Bullen, T. (1984). Chromian spinel as a petrogenetic indicator in abyssal and alpine-type peridotites and spatially associated lavas. *Contributions to Mineralogy and Petrology*, *86*, 54–76. https://doi.org/10.1007/BF00373711

Dijkstra, A., Drury, M. R., Vissers, R., & Newman, J. (2002). On the role of melt-rock reaction in mantle shear zone formation in the Othris Peridotite Massif (Greece). *Journal of Structural Geology*, *24*, 1431–1450. https://doi.org/10.1016/S0191-8141(01)00142-0

DOWNES, H. (2001). Formation and Modification of the Shallow Sub-continental Lithospheric Mantle: A Review of Geochemical Evidence from Ultramafic Xenolith Suites and Tectonically Emplaced Ultramafic Massifs of Western and Central Europe. *Journal of Petrology*, *42*(1), 233–250. https://doi.org/10.1093/petrology/42.1.233

Droop, G. T. R. (1987). A general equation for estimating Fe^{3+} concentrations in ferromagnesian silicates and oxides from microprobe analyses, using stoichiometric criteria. *Mineralogical Magazine*, *51*(361), 431–435. https://doi.org/10.1180/minmag.1987.051.361.10

Dubacq, B., Soret, M., Jewison, E., & Agard, P. (2019). Early subduction dynamics recorded by the metamorphic sole of the Mt. Albert ophiolitic complex (Gaspé, Quebec). *Lithos*, *334–335*, 161–179. https://doi.org/10.1016/j.lithos.2019.03.019

Franqui, N. O. C., Choi, S. H., & Lee, D.-C. (2017). Peridotites and basaltic rocks within an ophiolitic mélange from the SW igneous province of Puerto Rico: Relation to the

evolution of the Caribbean Plate. *Geological Magazine*, *154*(1), 96–118. https://doi.org/10.1017/S001675681500093X

Gaetani, G. A., & Grove, T. L. (1998). The influence of water on melting of mantle peridotite. *Contributions to Mineralogy and Petrology*, *131*(4), 323–346. https://doi.org/10.1007/s004100050396

Govindaraju, K. (1994). 1994 Compilation of Working Values and Sample Description for 383 Geostandards. *Geostandards Newsletter*, *18*(S1), 1–158. https://doi.org/10.1046/j.1365-2494.1998.53202081.x-i1

Hattori, K., Takahashi, Y., Guillot, S., & Johanson, B. (2005). Occurrence of arsenic (V) in forearc mantle serpentinites based on X-ray absorption spectroscopy study. *Geochimica et Cosmochimica Acta*, *69*(23), 5585–5596. https://doi.org/10.1016/j.gca.2005.07.009

Hellebrand, E., Snow, J. E., Dick, H. J. B., & Hofmann, A. W. (2001). Coupled major and trace elements as indicators of the extent of melting in mid-ocean-ridge peridotites. *Nature*, *410*(6829), 677–681. Scopus. https://doi.org/10.1038/35070546

Hicks, S. P., Bie, L., Rychert, C. A., Harmon, N., Goes, S., Rietbrock, A., Wei, S. S., Collier, J. S., Henstock, T. J., Lynch, L., Prytulak, J., Macpherson, C. G., Schlaphorst, D., Wilkinson, J. J., Blundy, J. D., Cooper, G. F., Davy, R. G., Kendall, J.-M., & VoiLA Working Group. (2023). Slab to back-arc to arc: Fluid and melt pathways through the mantle wedge beneath the Lesser Antilles. *Science Advances*, *9*(5), eadd2143. https://doi.org/10.1126/sciadv.add2143

Hidas, K., Tommasi, A., Garrido, C. J., Padrón-Navarta, J. A., Mainprice, D., Vauchez, A., Barou, F., & Marchesi, C. (2016). Fluid-assisted strain localization in the shallow subcontinental lithospheric mantle. *Lithos*, *262*, 636–650. https://doi.org/10.1016/j.lithos.2016.07.038

Hirth, G., & Guillot, S. (2013). Rheology and Tectonic Significance of Serpentinite. *Elements*, *9*(2), 107–113. https://doi.org/10.2113/gselements.9.2.107

Jochum, K. P., McDonough, W. F., Palme, H., & Spettel, B. (1989). Compositional constraints on the continental lithospheric mantle from trace elements in spinel peridotite xenoliths. *Nature*, *340*(6234), Article 6234. https://doi.org/10.1038/340548a0

Kodolányi, J., Pettke, T., Spandler, C., Kamber, B. S., & Gméling, K. (2012). Geochemistry of Ocean Floor and Fore-arc Serpentinites: Constraints on the Ultramafic Input to Subduction Zones. *Journal of Petrology*, *53*(2), 235–270. https://doi.org/10.1093/petrology/egr058

MacGregor, I. D., & Basu, A. R. (1979). Petrogenesis of the Mount Albert Ultramafic Massif, Quebec: Summary. *GSA Bulletin*, *90*(10), 898–900. https://doi.org/10.1130/0016-7606(1979)90<898:POTMAU>2.0.CO;2

Maffione, M., Thieulot, C., van Hinsbergen, D. J. J., Morris, A., Plümper, O., & Spakman, W. (2015). Dynamics of intraoceanic subduction initiation: 1. Oceanic detachment fault inversion and the formation of supra-subduction zone ophiolites. *Geochemistry, Geophysics, Geosystems*, *16*(6), 1753–1770. https://doi.org/10.1002/2015GC005746

Malo, M., Ruffet, G., Pincivy, A., & Tremblay, A. (2008). A 40Ar/39Ar study of oceanic and continental deformation processes during an oblique collision: Taconian orogeny in the Quebec reentrant of the Canadian Appalachians. *Tectonics*, *27*(4). https://doi.org/10.1029/2006TC002094

Martin, C., Flores, K. E., Vitale-Brovarone, A., Angiboust, S., & Harlow, G. E. (2020). Deep mantle serpentinization in subduction zones: Insight from in situ B isotopes in slab and mantle wedge serpentinites. *Chemical Geology*, *545*, 119637. https://doi.org/10.1016/j.chemgeo.2020.119637

McDonough, W. F., & Sun, S. -s. (1995). The composition of the Earth. *Chemical Geology*, *120*(3), 223–253. https://doi.org/10.1016/0009-2541(94)00140-4

Niu, Y. (2004). Bulk-rock Major and Trace Element Compositions of Abyssal Peridotites: Implications for Mantle Melting, Melt Extraction and Post-melting Processes Beneath Mid-Ocean Ridges. *Journal of Petrology*, *45*(12), 2423–2458. https://doi.org/10.1093/petrology/egh068

O'Beirne-Ryan, A. M., Jamieson, R. A., & Gagnon, Y. D. (1990). Petrology of garnet–clinopyroxene amphibolites from Mont Albert, Gaspé, Quebec. *Canadian Journal of Earth Sciences*, *27*(1), 72–86. https://doi.org/10.1139/e90-006

Pagé, P., Bédard, J. H., Schroetter, J.-M., & Tremblay, A. (2008). Mantle petrology and mineralogy of the Thetford Mines Ophiolite Complex. *Lithos*, *100*(1), 255–292. https://doi.org/10.1016/j.lithos.2007.06.017

Paulick, H., Bach, W., Godard, M., De Hoog, J. C. M., Suhr, G., & Harvey, J. (2006). Geochemistry of abyssal peridotites (Mid-Atlantic Ridge, 15°20'N, ODP Leg 209): Implications for fluid/rock interaction in slow spreading environments. *Chemical Geology*, *234*(3), 179–210. https://doi.org/10.1016/j.chemgeo.2006.04.011

Pearce, J. A. (1982). Trace element characteristics of lavas from destructive plate boundaries. In R. S. Thorpe (Ed.), *Orogenic andesites and related rocks* (pp. 528–548). John Wiley and Sons. https://orca.cardiff.ac.uk/id/eprint/8625/

Pearce, J. A., & Norry, M. J. (1979). Petrogenetic implications of Ti, Zr, Y, and Nb variations in volcanic rocks. *Contributions to Mineralogy and Petrology*, *69*(1), 33–47. https://doi.org/10.1007/BF00375192

Perkins, D., & Anthony, E. (2011). The evolution of spinel lherzolite xenoliths and the nature of the mantle at Kilbourne Hole, New Mexico. *Contributions to Mineralogy and Petrology*, *162*, 1139–1157. https://doi.org/10.1007/s00410-011-0644-1

Perrot, M. G., De Souza, S., & Tremblay, A. (2021). From obduction to collision: A transect across Ordovician to Devonian sedimentary basins of the Québec Appalachians, Canada. In B. L. Cousens & N. Riggs (Eds.), *GSA in the Field in 2020* (Vol. 60, p. 0). Geological Society of America. https://doi.org/10.1130/2020.0060(02)

Perrot, M., Tremblay, A., & David, J. (2017). Detrital zircon U-Pb geochronology of the Magog Group, southern Quebec—Stratigraphic and tectonic implications for the Quebec Appalachians. *American Journal of Science*, *317*, 1049–1094. https://doi.org/10.2475/10.2017.01

Peters, D., Bretscher, A., John, T., Scambelluri, M., & Pettke, T. (2017). Fluid-mobile elements in serpentinites: Constraints on serpentinisation environments and element cycling in subduction zones. *Chemical Geology*, *466*, 654–666. https://doi.org/10.1016/j.chemgeo.2017.07.017

Plank, T., & Langmuir, C. H. (1993). Tracing trace elements from sediment input to volcanic output at subduction zones. *Nature*, *362*(6422), Article 6422. https://doi.org/10.1038/362739a0

Prigent, C., Guillot, S., Agard, P., & Ildefonse, B. (2018). Fluid-Assisted Deformation and Strain Localization in the Cooling Mantle Wedge of a Young Subduction Zone (Semail Ophiolite). *Journal of Geophysical Research: Solid Earth*, *123*(9), 7529–7549. https://doi.org/10.1029/2018JB015492

Prigent, C., Guillot, S., Agard, P., Lemarchand, D., Soret, M., & Ulrich, M. (2018). Transfer of subduction fluids into the deforming mantle wedge during nascent subduction: Evidence from trace elements and boron isotopes (Semail ophiolite, Oman). *Earth and Planetary Science Letters*, *484*, 213–228. https://doi.org/10.1016/j.epsl.2017.12.008

Reichen, L. E., & Fahey, J. J. (1962). *An improved method for the determination of FeO in rocks and minerals including garnet* [Pp. 1-5]. U.S. Geological Survey Bulletin 1144B. https://pubs.er.usgs.gov/publication/b1144B

Scambelluri, M., Cannaò, E., & Gilio, M. (2019). The water and fluid-mobile element cycles during serpentinite subduction. A review. *European Journal of Mineralogy*, 405–428. https://doi.org/10.1127/ejm/2019/0031-2842

Scambelluri, M., Fiebig, J., Malaspina, N., Müntener, O., & Pettke, T. (2004). Serpentinite Subduction: Implications for Fluid Processes and Trace-Element Recycling. *International Geology Review*, *46*(7), 595–613. https://doi.org/10.2747/0020-6814.46.7.595

Scambelluri, M., Müntener, O., Hermann, J., Piccardo, G. B., & Trommsdorff, V. (1995). Subduction of water into the mantle: History of an Alpine peridotite. *Geology*, *23*(5), 459–462. https://doi.org/10.1130/0091-7613(1995)023<0459:SOWITM>2.3.CO;2

Schumacher, J. (1991). Empirical Ferric Iron Corrections: Necessity, Assumptions, and Effects on Selected Geothermobarometers. *Mineralogical Magazine - MINER MAG*, *55*, 3–18. https://doi.org/10.1180/minmag.1991.055.378.02

Shervais, J. W. (1982). Ti-V plots and the petrogenesis of modern and ophiolitic lavas. *Earth and Planetary Science Letters*, *59*(1), 101–118. https://doi.org/10.1016/0012-821X(82)90120-0

Snow, J. E., & Dick, H. J. B. (1995). Pervasive magnesium loss by marine weathering of peridotite. *Geochimica et Cosmochimica Acta*, *59*(20), 4219–4235. https://doi.org/10.1016/0016-7037(95)00239-V

Souza, S., Tremblay, A., Ruffet, G., & Pinet, N. (2011). Ophiolite obduction in the Quebec Appalachians, Canada—40Ar/39Ar age constraints and evidence for syn-tectonic erosion and sedimentation123. *Canadian Journal of Earth Sciences*, *49*, 91–110.

Staal, C., & Barr, S. (2012). Lithospheric architecture and tectonic evolution of the Canadian Appalachians and associated Atlantic margin. *Geological Association of Canada, Special Paper*, *49*, 41–95.

Stern, F. G. (2013). *Geochemistry of the Ultramafic Rocks from the Bay of Island Ophiolitic Complex, Newfoundland.* [Thesis, Université d'Ottawa / University of Ottawa]. https://doi.org/10.20381/ruor-3000

Stuart, C. A., Meek, U., Daczko, N. R., Piazolo, S., & Huang, J.-X. (2018). Chemical Signatures of Melt–Rock Interaction in the Root of a Magmatic Arc. *Journal of Petrology*, *59*(2), 321–340. https://doi.org/10.1093/petrology/egy029

Takazawa, E., Okayasu, T., & Satoh, K. (2003). Geochemistry and origin of the basal lherzolites from the northern Oman ophiolite (northern Fizh block). *Geochemistry Geophysics Geosystems - GEOCHEM GEOPHYS GEOSYST*, *4*. https://doi.org/10.1029/2001GC000232

Tommasi, A., & Vauchez, A. (2015). Heterogeneity and anisotropy in the lithospheric mantle. *Tectonophysics*, *661*, 11–37. https://doi.org/10.1016/j.tecto.2015.07.026

Tremblay, A., & Pinet, N. (1994). Distribution and characteristics of Taconian and Acadian deformation, southern Québec Appalachians | GSA Bulletin | GeoScienceWorld. *GSA BUlletin*, *109*(6), 1172–1181.

Tremblay, A., & Pinet, N. (2016). Late Neoproterozoic to Permian tectonic evolution of the Quebec Appalachians, Canada. *Earth-Science Reviews*, *160*, 131–170. https://doi.org/10.1016/j.earscirev.2016.06.015

Tremblay, A., Ruffet, G., & Bédard, J. H. (2011). Obduction of Tethyan-type ophiolites—A case-study from the Thetford-Mines ophiolitic Complex, Quebec Appalachians, Canada. *Lithos*, *125*(1), 10–26. https://doi.org/10.1016/j.lithos.2011.01.003

Ulmer, P. (2001). Partial melting in the mantle wedge—The role of H2O in the genesis of mantle-derived 'arc-related' magmas. *Physics of the Earth and Planetary Interiors*, *127*, 215–232. https://doi.org/10.1016/S0031-9201(01)00229-1

Ulrich, M., Munoz, M., Boulvais, P., Cathelineau, M., Cluzel, D., Guillot, S., & Picard, C. (2020). Serpentinization of New Caledonia peridotites: From depth to (sub-)surface. *Contributions to Mineralogy and Petrology*, *75*(9), 91. https://doi.org/10.1007/s00410-020-01713-0

Üner, T., & Çakir, Ü. (2011). Mineralogical, Petrographical and Geochemical Characteristics of Eldivan Ophiolite (Çankırı) Harzburgitic Tectonites. *Mineral Res. Expl. Bull*, *143*, 75–94.

Wada, I., Rychert, C. A., & Wang, K. (2011). Sharp thermal transition in the forearc mantle wedge as a consequence of nonlinear mantle wedge flow: SHARP THERMAL TRANSITION IN THE WEDGE. *Geophysical Research Letters*, *38*(13), n/a-n/a. https://doi.org/10.1029/2011GL047705

Warren, J. (2016). Global Variations in Abyssal Peridotite Compositions. *Lithos*, *248*. https://doi.org/10.1016/j.lithos.2015.12.023

Warren, J. M., & Shimizu, N. (2010). Cryptic Variations in Abyssal Peridotite Compositions: Evidence for Shallow-level Melt Infiltration in the Oceanic Lithosphere. *Journal of Petrology*, *51*(1–2), 395–423. https://doi.org/10.1093/petrology/egp096

Whitehead, J., Reynolds, P. H., & Spray, J. G. (1995). The sub-ophiolitic metamorphic rocks of the Québec Appalachians. *Journal of Geodynamics*, *19*(3), 325–350. https://doi.org/10.1016/0264-3707(94)00021-M

Williams, H. (1979). Appalachian Orogen in Canada. *Canadian Journal of Earth Sciences*, *16*(3), 792–807. https://doi.org/10.1139/e79-070

Wintsch, R. P., Christoffersen, R., & Kronenberg, A. K. (1995). Fluid-rock reaction weakening of fault zones. *Journal of Geophysical Research: Solid Earth*, *100*(B7), 13021–13032. https://doi.org/10.1029/94JB02622

Yamaoka, K., Ishikawa, T., Matsubaya, O., Ishiyama, D., Nagaishi, K., Hiroyasu, Y., Chiba, H., & Kawahata, H. (2012). Boron and oxygen isotope systematics for a complete section of

oceanic crustal rocks in the Oman ophiolite. *Geochimica et Cosmochimica Acta*, *84*, 543–559. https://doi.org/10.1016/j.gca.2012.01.043

Yoder, H. S., JR., & Tilley, C. E. (1962). Origin of Basalt Magmas: An Experimental Study of Natural and Synthetic Rock Systems. *Journal of Petrology*, *3*(3), 342–532. https://doi.org/10.1093/petrology/3.3.342

Yoshikawa, M., Python, M., Tamura, A., Arai, S., Takazawa, E., Shibata, T., Ueda, A., & Sato, T. (2015). Melt extraction and metasomatism recorded in basal peridotites above the metamorphic sole of the northern Fizh massif, Oman ophiolite. *Tectonophysics*, *650*, 53–64. https://doi.org/10.1016/j.tecto.2014.12.004

Supplementary Figures and Tables

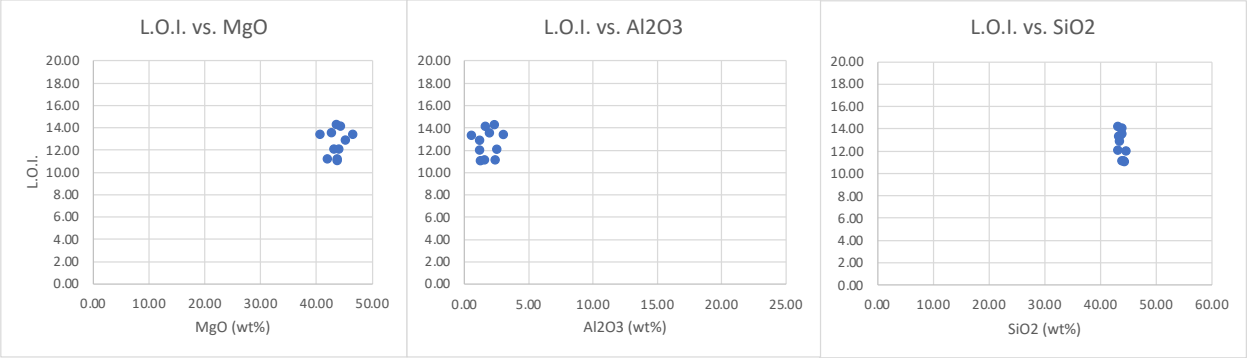

Fig 1 Major elements against L.O.I content cluster together indicating no to limited major element mobility during serpentinization.

Table 1
Relevant correlations of all measured trace elements with major element MgO, HFSEs (Ti and Nb) and HREE (Er).

		Major element	HFSE			HREE	
	Element	Correlations MgO	Correlations Ti	Correlations Zr	Correlations Nb	Correlations Er	Correlation Yb
	Si		0.61	0.00	0.27	0.59	0.47
	Ca		0.71	0.01	0.05	0.66	0.63
	Sc		0.91	0.53	0.35	0.89	0.89
HFSE	Ti		1.00	0.65	0.36	0.91	0.91
	V		0.72	0.18	0.48	0.77	0.82
	Cr		0.59	0.07	0.47	0.79	0.70
	Mn		0.32	0.56	0.22	0.32	0.49
	Co		-0.22	-0.22	0.28	-0.01	-0.24
	Ni		-0.33	-0.36	0.12	-0.17	-0.19
	Cu		0.17	-0.03	0.41	0.29	0.23
	Zn		0.19	-0.18	0.16	0.35	0.32
	Ga		0.84	0.27	0.23	0.85	0.85
FME	As		0.34	-0.09	0.21	0.57	0.47
FME	Rb		0.43	-0.13	0.41	0.45	0.31
FME	Sr		0.71	0.35	-0.02	0.57	0.77
	Y		0.95	0.71	0.39	0.89	0.92
HFSE	Zr		0.65	1.00	0.37	0.49	0.57
HFSE	Nb		0.36	0.37	1.00	0.52	0.41
	Mo		0.33	0.09	0.08	0.27	0.47
FME	Cs		-0.02	0.73	0.25	-0.37	0.16
FME	Ba		0.60	0.11	-0.18	0.61	0.71
LREE	La	-0.59	0.52	-0.01	0.42	0.65	0.40
LREE	Ce	-0.28	0.30	0.12	0.44	0.28	0.32
LREE	Pr		0.16	-0.45	-0.19	-0.08	0.14
LREE	Nd	-0.14	0.34	0.61	0.22	0.16	0.30
MREE	Sm	0.17	0.09	0.14	0.27	0.15	0.01
MREE	Eu	1.00	-1.00	1.00	-1.00	-1.00	-1.00
MREE	Gd	0.09	-0.59	-0.93	0.04	-0.44	-0.67
HREE	Tb	-0.52	0.91	0.66	0.06	0.84	0.80
HREE	Dy	-0.92	0.94	0.55	0.36	0.84	0.96
HREE	Ho	-0.66	0.97	0.65	0.26	0.91	0.89
HREE	Er	-0.69	0.91	0.49	0.52	1.00	0.88
HREE	Yb	-0.79	0.91	0.57	0.41	0.88	1.00
HREE	Lu	-0.80	0.22	0.02	-0.04	0.24	0.19
HFSE	Hf		0.14	0.16	-0.26	0.22	-0.09
HFSE	Ta		-0.04	-0.57	0.27	0.21	-0.02
FME	Pb		0.18	0.37	-0.49	0.04	0.14
	Th		0.35	0.13	0.62	0.54	0.63
FME	U		0.06	0.15	0.07	-0.10	0.19